

Contents lists available at ScienceDirect

Petroleum Science

journal homepage: www.keaipublishing.com/en/journals/petroleum-science



Original Paper

Joint inversion with prestack waveform and spectral information for layered media



Zheng-Yang Kuai, Dan-Ping Cao*, Chao Jin

State Key Laboratory of Deep Oil and Gas, China University of Petroleum (East China), Qingdao, 266580, Shandong, China

ARTICLE INFO

Article history:
Received 5 November 2024
Received in revised form
28 April 2025
Accepted 9 June 2025
Available online 14 June 2025

Edited by Meng-Jiao Zhou

Keywords: Reflection matrix method Layered media Prestack inversion Time-frequency domain Joint inversion Bayesian inversion

ABSTRACT

Subsurface reservoirs commonly exhibit layered structures. Conventional amplitude variation with angle (AVA) inversion, which relies on the Zoeppritz equation and its approximations, often fails to accurately estimate elastic parameters because it assumes single-interface models and ignores multiple reflections and transmission losses. To address these limitations, this study proposes a novel prestack time-frequency domain joint inversion method that utilizes the reflection matrix method (RMM) as the forward operator. The RMM accurately simulates wave propagation in layered media, while the joint inversion framework minimizes the misfit between observed and synthetic data in both the time and frequency domains. By incorporating Bayesian theory to optimize the inversion process, the method effectively balances contributions from both time-domain waveforms and frequency-domain spectral information through a weighting factor. Tests on both synthetic data and field data demonstrate that the proposed method outperforms conventional AVA inversion and time-domain waveform inversion in accuracy and robustness. Furthermore, the method demonstrates good robustness against variations in initial models, random noise, and coherent noise interference. This study provides a practical and effective approach for high-precision reservoir characterization, with potential applications in complex layered media.

© 2025 The Authors. Publishing services by Elsevier B.V. on behalf of KeAi Communications Co. Ltd. This is an open access article under the CC BY-NC-ND license (http://creativecommons.org/licenses/by-nc-nd/4.0/).

1. Introduction

Amplitude variation with angle/offset (AVA/AVO) technology estimates subsurface elastic parameters by analyzing the variation of reflection amplitudes with offset or incident angle. This forms the foundation of prestack seismic inversion and plays a pivotal role in lithology identification, reservoir characterization and hydrocarbon detection. Conventional AVO/AVA inversion utilizes the Zoeppritz equation and its approximations (Aki and Richards, 2002; Shuey, 1985; Zoeppritz, 1919). However, these approximations reliance on the small-angle approximation, which often results in inaccurate results at larger incident angles (Mallick, 2007). Furthermore, these methods assume a single interface model, considering only primary reflection while neglecting transmission losses and multiple reflections. These simplifications limit their

E-mail address: caodp@upc.edu.cn (D.-P. Cao).

Peer review under the responsibility of China University of Petroleum (Beijing).

effectiveness to realistic layered media. These limitations can be effectively mitigated by employing more rigorous forward modeling methods approaches (Mallick and Adhikari, 2015; Sen and Roy, 2003).

To address the limitations of small-angle approximations, the exact Zoeppritz equation (Lu et al., 2015) offers an alternative solution. However, this approach still fails to account for the limitations imposed by wave propagation effects. In contrast, the reflection matrix method (RMM) grounded in plane wave theory provides a forward modeling technique for seismic wavefields in layered media. RMM utilizes a propagation matrix to connect the stress and displacement at the top and bottom of the layered medium, enabling accurate simulation of various propagation effects in layered media. RMM effectively captures complex wavefield characteristics, including aliasing effects in actual seismic gathers, thereby providing a robust theoretical foundation for detailed reservoir characterization. The RMM was initially proposed by Thomson (1950) to investigate elastic wave propagation in layered solid media and subsequently refined and extended by Haskell (1953). Gilbert and Backus (1966) formally defined the

^{*} Corresponding author.

"propagation matrix" as the transfer operator of stress and displacement between layers in a layered model. Fuchs (1968) pioneered the use of the Thomson-Haskell matrix to generate a synthetic seismogram incorporating all multiple reflections. Fuchs and Müller (1971) further enhanced the method by incorporating transmission loss into the forward modeling of layered media. They highlighted that RMM's key advantage lies in its ability to incorporate multiple reflections and converted waves within the reflection zone, yielding more accurate synthetic seismograms compared to ray-tracing methods. Kennett advanced the reflection matrix method by developing an iterative approach to calculate reflection and transmission coefficients for multilayer media. He also addressed the instability issues arising from exponential growth in the propagation matrix, leading to its widespread adoption in seismic data forward modeling (Kennett, 1974, 2009; Kennett and Kerry, 1979). These developments render RMM particularly suitable for modeling complex layered media and provide a robust foundation for joint time-frequency domain inversion. Subsequent research has further extended RMM to more complex media, including anisotropic and viscoelastic environments (Carcione, 1990; Fryer and Frazer, 1987).

Despite being the most widely adopted and successful reservoir characterization technique, the AVO inversion method exhibits limitations in its forward operator for layered media applications. Mallick and Adhikari (2015) developed a prestack waveform inversion method based on a locally horizontal one-dimensional (1D) layered structure assumption and conducted a comparative analysis with AVO inversion using genetic algorithm on actual seismic data. Their findings established that the prestack waveform inversion method delivers enhanced resolution and accuracy. Consequently, inversion algorithm employing RMM as the forward operator have emerged as the preferred approach for reservoir characterization. However, due to the computational complexity of forward modeling, many prestack waveform inversion methods rely on global optimization algorithms (Li and Mallick, 2015; Mallick, 1999; Mallick and Adhikari, 2015; Padhi and Mallick, 2014; Sen and Stoffa, 1991). Although these methods eliminate the need to compute derivatives of the objective function, the extensive forward modeling requirements impose substantial computational costs. To address these computational challenges, gradient-based optimization algorithms have been adopted in some prestack waveform inversion methods (Amundsen and Ursin, 1991; Lu et al., 2019; Sen and Roy, 2003; Yang and Wang, 2022; Yang and Lu, 2020; Zhao et al., 1994). The inherently illposed nature of prestack waveform inversion presents substantial challenges for traditional regularization approaches, often limiting their effectiveness. To mitigate solutions non-uniqueness in inverse problems, it is crucial to fully incorporate priori knowledge of the model parameters. The emergence of Bayesian framework-based prestack waveform inversion method has significantly enhanced the stability of the inversion process by effectively integrating prior information and observation data (Alemie and Sacchi, 2011; Buland and Omre, 2003; Liu et al., 2016; Luo et al., 2020).

The instability of inversion processes is further aggravated by insufficient input data. Recent studies demonstrate that PP-PS joint prestack waveform inversion substantially improves result reliability (Lu et al., 2015; Luo et al., 2020; Yang and Wang, 2022). However, both pure PP wave and PP-PS joint inversion predominantly focus on time-domain waveforms processing while overlooking critical frequency-domain information. As seismic waves propagate through layered media, they generate complex tuned reflections exhibiting distinct frequency-domain characteristics. Spectral characteristics offer key advantages for quantifying layered thickness in stratified formations (Marfurt and Kirlin,

2001; Partyka et al., 1999; Puryear and Castagna, 2008). Therefore, integrating frequency-domain information into time-domain waveform inversion can effectively mitigate the multi-solution problem, enhance inversion stability, and improve result reliability. Rubino and Velis (2009) introduced prestack amplitude spectral inversion for thin-layer characterization, demonstrating that frequency-domain spectral data can accurately resolve thin layers below the tuning thickness. Lin et al. (2023) observed that frequency-domain inversion achieve higher resolution at fine feature scale but exhibits reduced stability under high-noise conditions. Time-domain waveform inversion maintains noise robustness at low signal-to-noise ratios (SNR) but has inherent resolution limits (Yin et al., 2017). Time-frequency domain joint inversion effectively balances noise robustness and resolution, producing superior inversion results (Lin et al., 2023; Yin et al., 2017; Zhao et al., 2023).

This study utilizes the RMM as the forward operator to generate both synthetic angle gathers and frequency amplitude spectral data. We develop a prestack time-frequency joint inversion algorithm incorporating the Gauss-Newton method within a Bayesian framework to estimate P- and S-wave velocity and density parameters. The proposed method is validated using both onedimensional (1D) and two-dimensional (2D) model data, compare the AVO inversion method based on the Aki approximation, the time-domain waveform inversion method using RMM, and the time-frequency domain joint inversion method based on RMM. Furthermore, this study systematically examines the impacts of initial model variations, random noise, and coherent noise on the proposed inversion method, demonstrating its excellent stability. Finally, the reliability and robustness of the proposed method are demonstrated through its application to field seismic data.

2. Method

2.1. Forward operator

Grounded in plane wave theory, the RMM characterizes wave propagation in horizontally layered, homogeneous media. This method efficiently simulates all propagation phenomena in layered systems, including reflected, transmitted, and multiple waves, as well as other physical effects. For an isotropic layered media, the wave propagation can be described by the following ordinary differential equation (Kennett, 2009):

$$\partial_{\mathbf{z}}\mathbf{b} = i\omega\mathbf{A}\mathbf{b} + \mathbf{F},\tag{1}$$

where **b** denotes the stress-displacement vector, **F** represents the body force term, **A** is the system matrix, i is the imaginary unit, and the ω denotes the angular frequency. The RMM utilizes the eigenvector matrix **D** of the system matrix and the phase shift matrix **E** of the upgoing and downgoing waves between layers to obtain the wave propagation matrix **Q** of the entire layer system:

$$\mathbf{Q} = \mathbf{D}_1^{-1} \prod_{k=2}^{i-1} \left(\mathbf{D}_k \mathbf{E}_k \mathbf{D}_k^{-1} \right) \mathbf{D}_n, \tag{2}$$

where subscripts the position of the layer. Using the block matrix, **Q** can be written as follows:

$$\mathbf{Q} = \begin{bmatrix} \mathbf{Q}_{UU} & \mathbf{Q}_{UD} \\ \mathbf{Q}_{DU} & \mathbf{Q}_{DD} \end{bmatrix}. \tag{3}$$

The reflection and transmission coefficient matrix of the entire layer system can be expressed by this block matrix:

$$\begin{aligned} & \mathbf{R}_{D} = \mathbf{Q}_{UD}(\mathbf{Q}_{DD})^{-1}, \mathbf{R}_{U} = -(\mathbf{Q}_{DD})^{-1}\mathbf{Q}_{DU}, \\ & \mathbf{T}_{D} = (\mathbf{Q}_{DD})^{-1}, \mathbf{T}_{U} = \mathbf{Q}_{UU} - \mathbf{Q}_{UD}(\mathbf{Q}_{DD})^{-1}\mathbf{Q}_{DU}. \end{aligned} \tag{4}$$

The reflection coefficient matrix can be expressed as \mathbf{R}_D =

$$egin{bmatrix} R_D^{PP} & R_D^{PS} \\ R_D^{SP} & R_D^{SS} \end{bmatrix}$$
, and the reflection coefficient in the frequency-

slowness domain is obtained. As shown in Fig. 1, it is a schematic diagram of the reflection and transmission of three-layer model in an elastic media, where α, β, ρ, h represent the P- and S-wave velocity, density and layer thickness respectively, $R_{\rm PP}, R_{\rm PS}, T_{\rm PP}, T_{\rm PS}$ at the interface represent the reflected and transmitted PP and PS waves. The dotted arrows in the middle layer represent multiple reflections in the three-layer model.

The frequency-slowness domain reflection coefficient $\mathbf{R}(\omega,p)$ obtained in Eq. (4) needs to be converted to the frequency-angle domain $\mathbf{R}(\omega,\theta)$. Then the frequency domain wavelet \mathbf{W} is multiplied by the frequency domain reflection coefficient to obtain the reflection coefficient spectral $\mathbf{A}(\omega,\theta)$, and the time domain angle gather \mathbf{d}_{PP} is obtained by inverse Fourier transform:

$$\mathbf{A}(\omega,\theta) = \mathbf{R}(\omega,\theta) \cdot \mathbf{W}(\omega,\theta),\tag{5}$$

$$\mathbf{d}_{\mathrm{PP}} = \frac{1}{2\pi} \int_{-\infty}^{\infty} \mathbf{A}(\omega, \theta) \mathrm{e}^{\mathrm{i}\omega t} \mathrm{d}\omega. \tag{6}$$

2.2. Joint inversion objective function

The time-domain waveform and frequency-domain spectral can be expressed as:

$$\mathbf{d}_{t} = \mathbf{G}_{t}(\mathbf{m}) + \mathbf{n}_{t}, \quad \mathbf{d}_{f} = \mathbf{G}_{f}(\mathbf{m}) + \mathbf{n}_{f}, \tag{7}$$

where \mathbf{d}_t represents the prestack time-domain waveform data, \mathbf{d}_f represents the prestack frequency-domain amplitude spectral data. \mathbf{n}_t and \mathbf{n}_f represent the random noise of observation data in time domain and frequency domain respectively. \mathbf{G} represents the nonlinear forward operator, and \mathbf{m} represents elastic parameters such as P- and S-wave velocity and density, which can be expressed as $\mathbf{m} = [\alpha_1 \cdots \alpha_N, \beta_1 \cdots \beta_N, \rho_1 \cdots \rho_N]^T$. AVO inversion is inherently ill-posed without prior constraints. To address this, we develop a Bayesian framework-based prestack joint inversion method. Assuming that the noises \mathbf{n}_t and \mathbf{n}_f obey Gaussian distribution and the noises are independent of each other, the like-lihood function can be written as:

$$P(\mathbf{d}_{t}|\mathbf{m}) = \exp\left(-\frac{1}{2}(\mathbf{d}_{t} - \mathbf{G}_{t}(\mathbf{m}))^{T}\mathbf{C}_{t}^{-1}(\mathbf{d}_{t} - \mathbf{G}_{t}(\mathbf{m}))\right), \tag{8}$$

$$P\Big(\boldsymbol{d}_f|\boldsymbol{m}\Big) = exp\bigg(-\frac{1}{2}\Big(\boldsymbol{d}_f - \boldsymbol{G}_f(\boldsymbol{m})\Big)^T\boldsymbol{C}_f^{-1}\Big(\boldsymbol{d}_f - \boldsymbol{G}_f(\boldsymbol{m})\Big)\bigg), \tag{9}$$

where \mathbf{C}_{t} and \mathbf{C}_{f} represent the variance of noise, when it is assumed that the noises in seismic records are independent of each other, there is $\mathbf{C} = \sigma^2 \mathbf{I}$. At the same time, assuming that the prior distribution also obeys Gaussian distribution, there are

$$P(\mathbf{m}) = \exp\left(-\frac{1}{2} (\mathbf{m} - \mathbf{u})^{T} \mathbf{C}_{m}^{-1} (\mathbf{m} - \mathbf{u})\right), \tag{10}$$

where \mathbf{u} in the prior distribution represents the mean value of the model, and $\mathbf{C}_{\mathrm{m}}^{-1}$ represents the inverse of covariance matrix of the model parameter \mathbf{m} , the covariance matrix can be expressed as:

$$\mathbf{C}_{m} = \operatorname{Kron}(\operatorname{Cov}\{\boldsymbol{\alpha}, \boldsymbol{\beta}, \boldsymbol{\rho}\}, \mathbf{I}), \tag{11}$$

where $\operatorname{Kron}(\cdot)$ is the Kronecker product, $\operatorname{Cov}(\cdot)$ is the covariance matrix. I is the identity matrix, size is $N \times N$, N is the length of parameter. The covariance matrix introduces the relationship between the parameters, significantly enhancing the numerical stability of inversion solutions. From this we can get that the posterior distribution is as follows:

$$\begin{split} P(\mathbf{m}|\mathbf{d}) = & P(\mathbf{d}|\mathbf{m})P(\mathbf{m}) \propto \exp\bigg\{ -\frac{1}{2} \bigg[\xi \bigg(\mathbf{d}_t - \mathbf{G}_t(\mathbf{m}) \bigg)^T \bigg(\mathbf{d}_t - \mathbf{G}_t(\mathbf{m}) \bigg) \\ & + (1 - \xi) \bigg(\mathbf{d}_f - \mathbf{G}_f(\mathbf{m}) \bigg)^T \bigg(\mathbf{d}_f - \mathbf{G}_f(\mathbf{m}) \bigg) \\ & + \eta (\mathbf{m} - \mathbf{u})^T \mathbf{C}_m^{-1} (\mathbf{m} - \mathbf{u}) \bigg] \bigg\}, \end{split}$$

$$(12)$$

where ξ denotes the time-frequency weighting factor and η represents the prior constraint regularization parameter. The parameter ξ balances the contributions of waveform and spectral information in the joint inversion process, while η regulates the trade-off between seismic data and prior information. Increasing η amplifies the prior constraint's impact, enhancing solution stability at the cost of resolution. Conversely, reducing η increases the detail resolution but enhances noise susceptibility. Typically, these weighting factors are determined through trial-and-error approaches based on model tests and well-log inversion analysis.

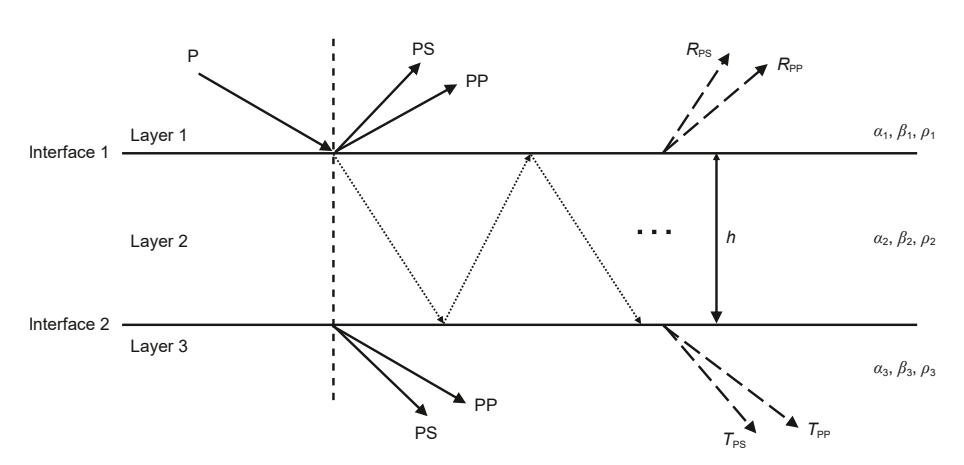


Fig. 1. Schematic diagram of reflection and transmission in a three-layer elastic media model.

Alternatively, they can be optimized using the L-curve method or generalized cross-validation to achieve an optimal trade-off.

Maximizing the posterior probability distribution is mathematically equivalent to minimizing the following objective function:

$$\begin{split} Q(\boldsymbol{m}) = & \frac{1}{2} \left[\xi \Big(\boldsymbol{d}_t - \boldsymbol{G}_t(\boldsymbol{m}) \Big)^T \Big(\boldsymbol{d}_t - \boldsymbol{G}_t(\boldsymbol{m}) \Big) + (1 - \xi) \Big(\boldsymbol{d}_f - \boldsymbol{G}_f(\boldsymbol{m}) \Big)^T \\ & \Big(\boldsymbol{d}_f - \boldsymbol{G}_f(\boldsymbol{m}) \Big) + \eta (\boldsymbol{m} - \boldsymbol{u})^T \boldsymbol{C}_m^{-1} (\boldsymbol{m} - \boldsymbol{u}) \right]. \end{split} \tag{13}$$

The Gauss-Newton method is particularly well-suited for solving nonlinear least squares problems, a common challenge in seismic inversion. In contrast to first-order optimization

algorithms (e.g., gradient descent), the Gauss-Newton method exhibits superior efficiency and stability by utilizing approximate second-order derivative information. Additionally, by incorporating prior information as constraints, the method effectively alleviates overfitting, yielding more reliable and physically meaningful solutions. These advantages solidify the Gauss-Newton method as an optimal choice for objective function optimization in this study:

$$\mathbf{m}^{k+1} = \mathbf{m}^k + \Delta \mathbf{m}, \Delta \mathbf{m} = -\mathbf{H} \left(\mathbf{m}^k \right)^{-1} \mathbf{g} \left(\mathbf{m}^k \right), \tag{14}$$

where **g** and **H** denote the gradient vector and Hessian matrix of the objective function respectively, defined as follows:

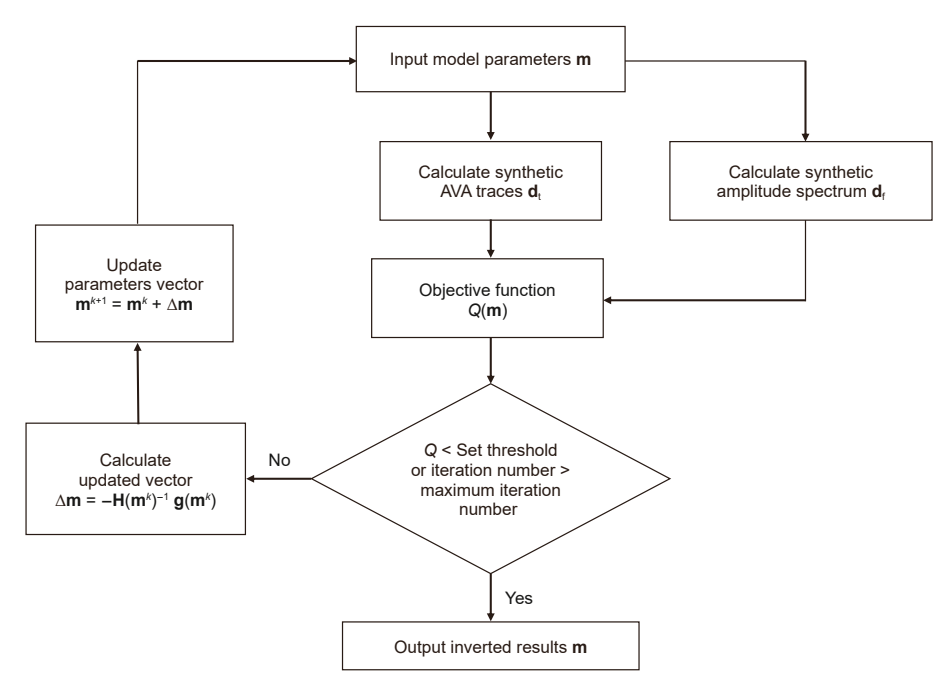


Fig. 2. Flow chart of prestack time-frequency domain joint inversion based on the RMM.

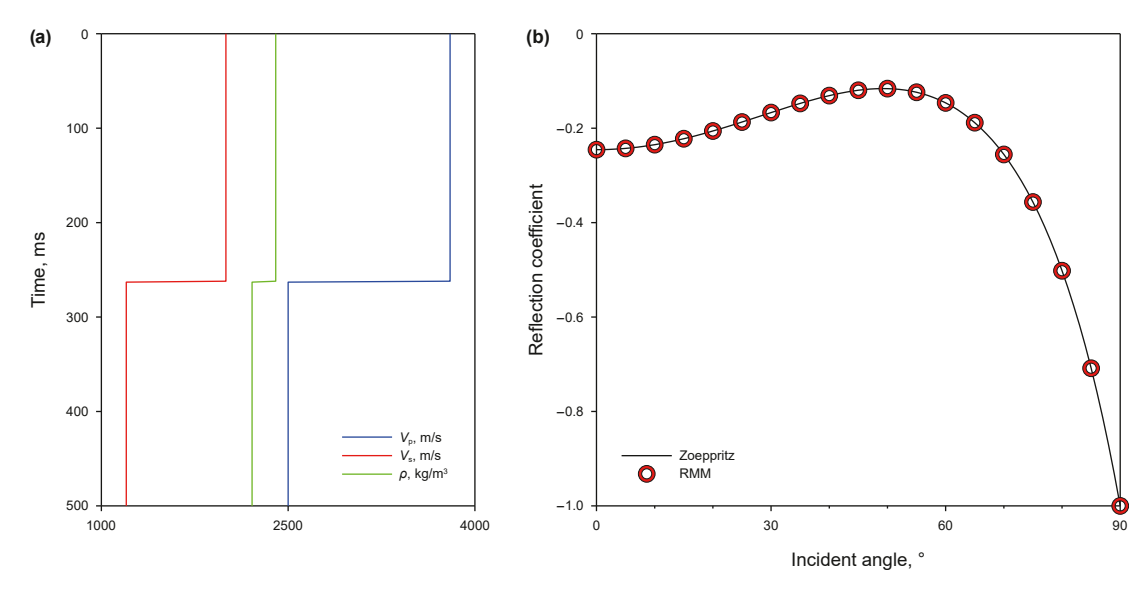


Fig. 3. (a) Single interface model, (b) comparison of PP wave reflection coefficients computed using the Zoeppritz equation (black solid line) and the RMM (red circles).

$$\mathbf{g}(\mathbf{m}) = \frac{\partial Q(\mathbf{m})}{\partial \mathbf{m}} = \xi \left(\frac{\partial \mathbf{G}_{t}(\mathbf{m})}{\partial \mathbf{m}}\right)^{T} (\mathbf{G}_{t}(\mathbf{m}) - \mathbf{d}_{t}) + (1 - \xi) \left(\frac{\partial \mathbf{G}_{f}(\mathbf{m})}{\partial \mathbf{m}}\right)^{T} \left(\mathbf{G}_{f}(\mathbf{m}) - \mathbf{d}_{f}\right) + \eta \mathbf{C}_{m}^{-1}(\mathbf{m} - \boldsymbol{\mu}). \tag{15}$$

$$\mathbf{H}(\mathbf{m}) = \frac{\partial^2 Q(\mathbf{m})}{\partial \mathbf{m}^2} \approx \xi \left(\frac{\partial \mathbf{G}_t(\mathbf{m})}{\partial \mathbf{m}}\right)^T \frac{\partial \mathbf{G}_t(\mathbf{m})}{\partial \mathbf{m}} + (1 - \xi) \left(\frac{\partial \mathbf{G}_f(\mathbf{m})}{\partial \mathbf{m}}\right)^T \frac{\partial \mathbf{G}_f(\mathbf{m})}{\partial \mathbf{m}} + \eta \mathbf{C}_m^{-1}. \tag{16}$$

Both the time-domain waveform and the frequency-domain spectral are related to the parameter \mathbf{m} through the reflection coefficient. Therefore, only the derivative of the reflection coefficient \mathbf{R}_{D} with respect to the parameter \mathbf{m} is required:

$$\begin{split} \frac{\partial \boldsymbol{R}_{D}}{\partial \boldsymbol{m}} &= \frac{\partial \left[\boldsymbol{Q}_{UD}(\boldsymbol{Q}_{DD})^{-1}\right]}{\partial \boldsymbol{m}} = \frac{\partial \boldsymbol{Q}_{UD}}{\partial \boldsymbol{m}}(\boldsymbol{Q}_{DD})^{-1} + \boldsymbol{Q}_{UD}\frac{\partial (\boldsymbol{Q}_{DD})^{-1}}{\partial \boldsymbol{m}} \\ &= \frac{\partial \boldsymbol{Q}_{UD}}{\partial \boldsymbol{m}}(\boldsymbol{Q}_{DD})^{-1} - \boldsymbol{Q}_{UD}(\boldsymbol{Q}_{DD})^{-1}\frac{\partial \boldsymbol{Q}_{DD}}{\partial \boldsymbol{m}}(\boldsymbol{Q}_{DD})^{-1}, \end{split} \tag{17}$$

convergence threshold is set to 0.01. To ensure computational efficiency and avoid unnecessary iterations, the optimization process is terminated if the objective function value increases or shows insufficient decrease for five consecutive iterations. These parameters were optimized through extensive testing to achieve an optimal balance between inversion accuracy and computational efficiency.

3. Synthetic data examples

3.1. Forward operator testing

$$\frac{\partial \mathbf{Q}}{\partial \mathbf{m}} = \frac{\partial \left(\mathbf{D}_{1}^{-1} \begin{bmatrix} \prod_{k=2}^{n-1} \mathbf{D}_{k} \mathbf{E}_{k} \mathbf{D}_{k}^{-1} \end{bmatrix} \mathbf{D}_{n} \right)}{\partial \mathbf{m}}$$

$$= \frac{\partial \left(\mathbf{D}_{1}^{-1}\right) \begin{bmatrix} \prod_{k=2}^{n-1} \mathbf{D}_{k} \mathbf{E}_{k} \mathbf{D}_{k}^{-1} \end{bmatrix} \mathbf{D}_{n}}{\partial m_{1}^{i}} + \mathbf{D}_{1}^{-1} \frac{\partial \left(\begin{bmatrix} \prod_{k=2}^{n-1} \mathbf{D}_{k} \mathbf{E}_{k} \mathbf{D}_{k}^{-1} \end{bmatrix} \right)}{\partial m_{k}^{i}} \mathbf{D}_{n} + \mathbf{D}_{1}^{-1} \begin{bmatrix} \prod_{k=2}^{n-1} \mathbf{D}_{k} \mathbf{E}_{k} \mathbf{D}_{k}^{-1} \end{bmatrix} \partial (\mathbf{D}_{n})}{\partial m_{n}^{i}}, \tag{18}$$

where $\frac{\partial \mathbf{Q}}{\partial \mathbf{m}}$ denotes the partial derivative of the wave propagation matrix \mathbf{Q} with respect to the elastic parameters \mathbf{m} across all layers in the layered medium. Fig. 2 illustrates the workflow of the RMM-based Bayesian prestack time-frequency joint inversion method. The maximum number of iterations is set to 25, and the

To assess the effectiveness of the RMM in AVA modeling and prestack inversion, we conducted numerical tests on both single-interface and multi-layer models. Fig. 3 presents a comparison of P-wave reflection coefficients computed for the interface. In Fig. 3 (a), the colored lines represent elastic parameters, while in Fig. 3

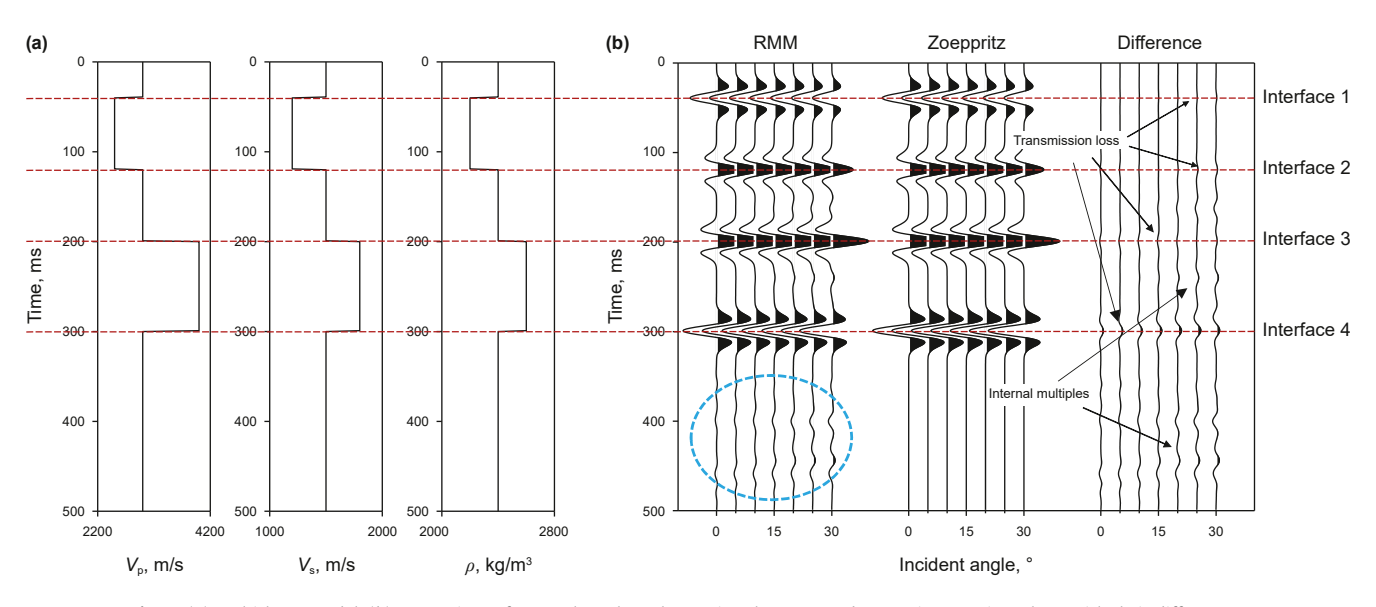


Fig. 4. (a) Multi-layer model, (b) comparison of prestack angle gathers using the RMM and Zoeppritz equation, along with their differences.

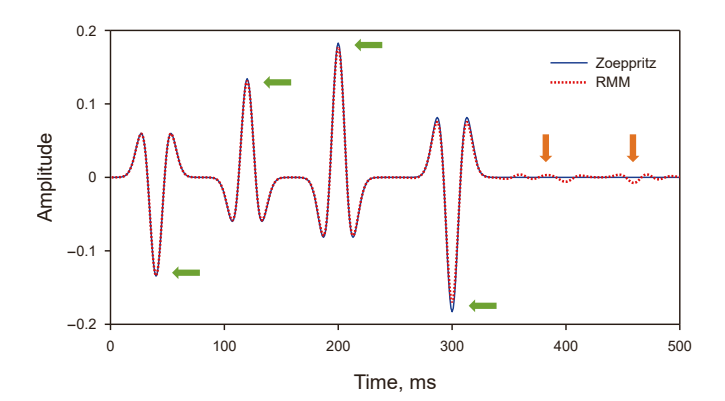


Fig. 5. Comparison of seismic waveforms at 0° incidence angle computed using the Zoeppritz equation (blue solid line) and RMM (red dashed line).

(b), the black solid line indicates the reflection coefficient computed by the Zoeppritz equation, and the red circles denote the reflection coefficient obtained from RMM. The results show excellent agreement between the reflection coefficients computed by both methods for the single-interface model.

Fig. 4 shows a comparison of time-domain angle gathers generated by the RMM and the Zoeppritz equation for a multilayer model using a 30 Hz Riker wavelet. Fig. 4(a) shows the elastic parameters, including P- and S-wave velocity, and density. Fig. 4(b) presents the time-domain angle gathers computed by both methods and their differences. Red dashed lines denote interfaces, blue dashed circles highlight multiple internal reflections, and arrows indicate transmission losses. It is evident that multiple reflections become more pronounced with increasing incident angle, while transmission losses grow more significant with increasing propagation time. The prestack time-domain angle gathers generated using the RMM account for more propagation effects.

Fig. 5 depicts the differences in seismic waveforms generated by the two methods at an incidence angle of 0°. The solid blue line represents the forward modeling results obtained by the Zoeppritz equation, while the red dashed lines denote the results calculated

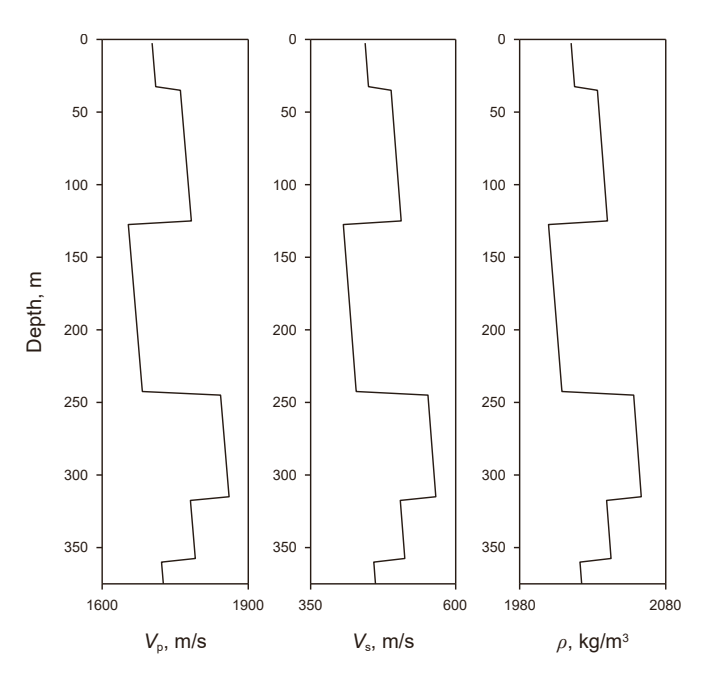


Fig. 7. Elastic parameters of 1D model: **(a)** P-wave velocity, **(b)** S-wave velocity and **(c)** density.

using the RMM. Green arrows highlight transmission losses, while orange arrows indicate multiple reflections. Evidently, transmission losses increase as propagation distance increases. Fig. 6 compares the amplitudes at interfaces 1 and 4 of the multilayer model. Fig. 6(a) shows the comparison result for interface 1, while Fig. 6(b) shows the result for interface 4. It is evident that transmission losses are more pronounced at interface 4 than at interface 1. These results indicate that the RMM, as a forward operator, offers better adaptability for modeling layered media. Therefore, using the RMM as the forward operator for prestack inversion can enhance the accuracy of elastic parameter predictions in layered media, especially in scenarios with complex wave propagation effects.

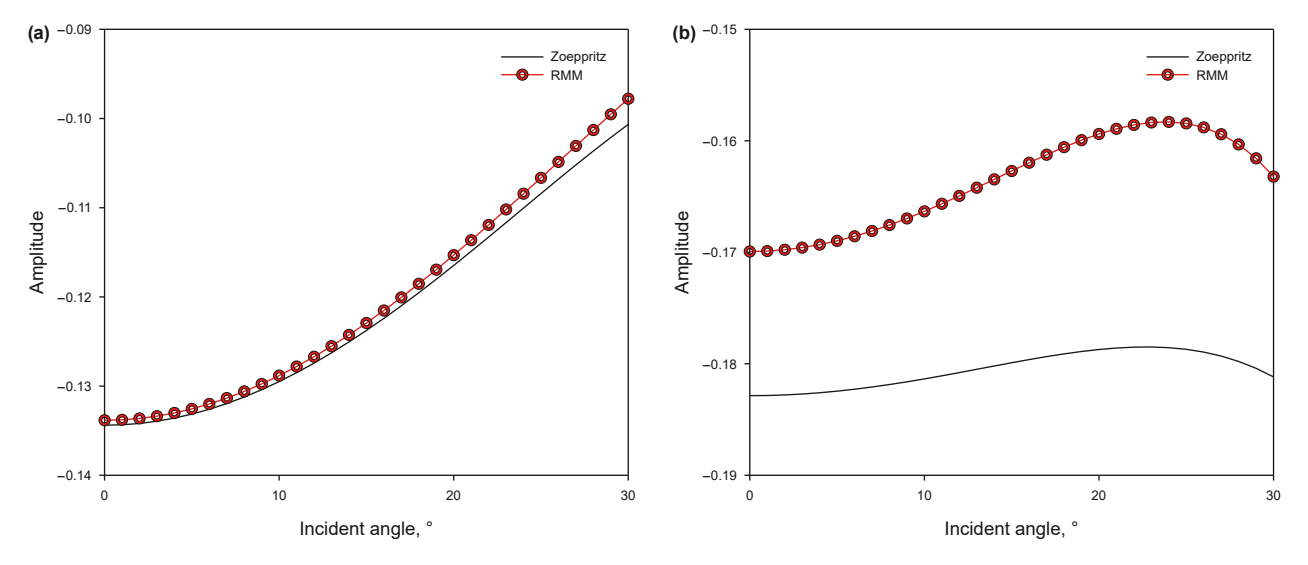


Fig. 6. Comparison of prestack angle gathers amplitudes at the interface computed using the Zoeppritz equation (black solid line) and RMM (red circles): (a) interface 1, (b) interface 4.

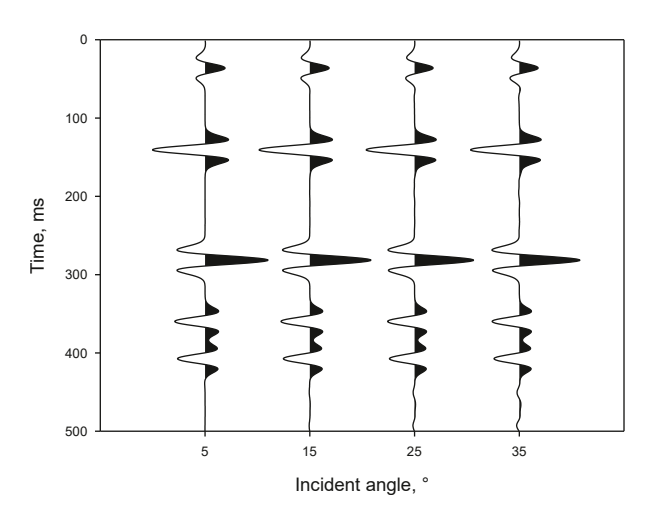


Fig. 8. Prestack synthetic angle gathers generated from the elastic parameters of 1D model

Table 1Mean squared error (MSE) between true model and inversion results of different methods.

MSE	$V_{\rm p}$ inversion	$V_{\rm s}$ inversion	ρ inversion
Aki approximation Time domain	135.98 15.95	83.98 9.46	12.75 1.50
Joint domain	0.17	0.10	0.016

3.2. Inversion algorithm testing

Following the validation of the RMM, we conducted prestack time-frequency domain joint inversion using 1-D model data. Fig. 7 displays the elastic parameters, including P- and S-wave velocity and density. First, prestack AVA gathers were generated as the observation data using a 30Hz Ricker wavelet, with incidence angles ranging from 5° to 35° at 10° interval, as shown in Fig. 8.

We compare the inversion results obtained using the Aki approximation, the time-domain waveform inversion results based on the RMM, and the time-frequency domain joint inversion

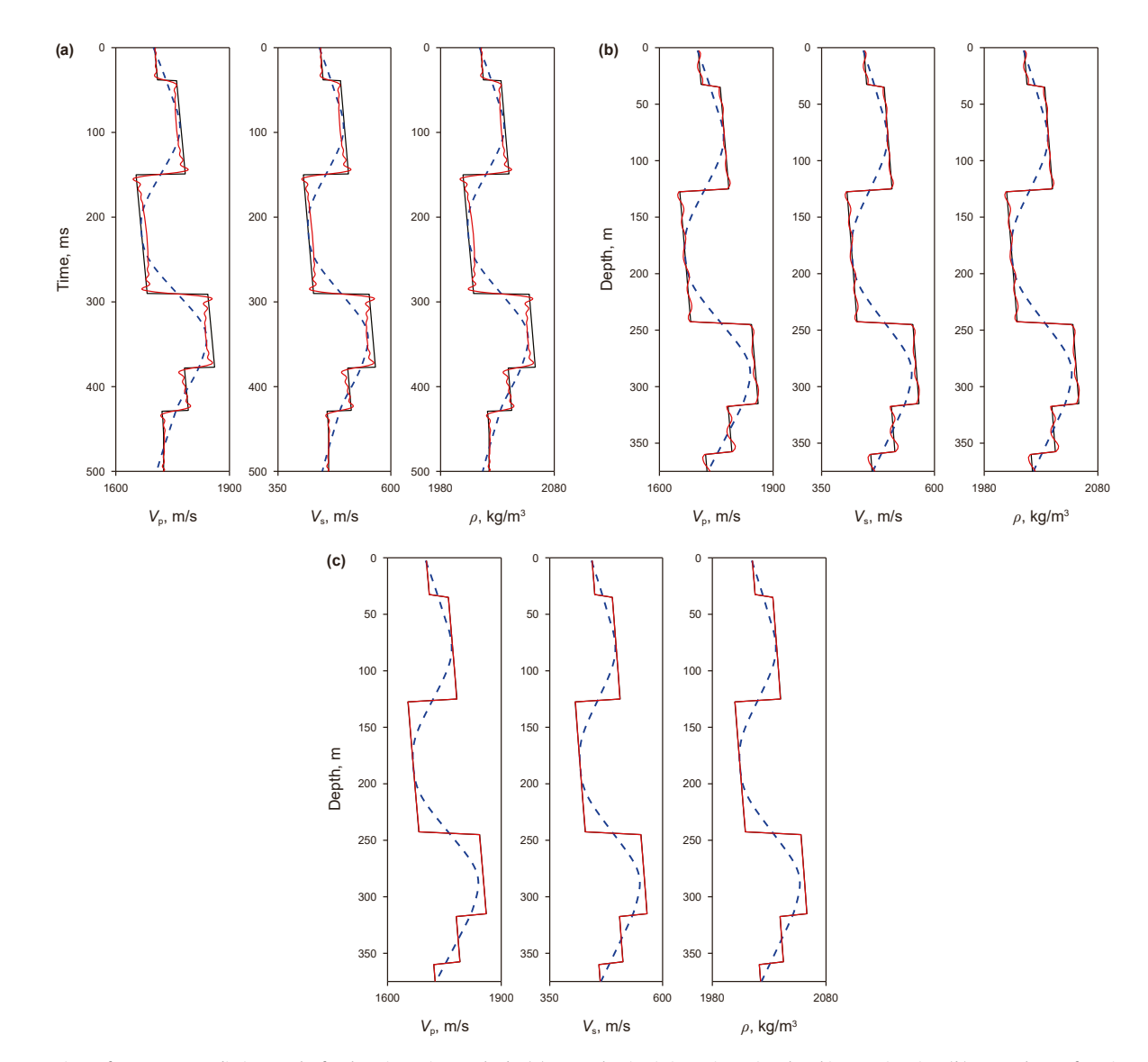


Fig. 9. Comparison of parameter prediction results for three inversion methods: (a) prestack seismic inversion using the Aki approximation, (b) prestack waveform inversion and (c) prestack time-frequency domain joint inversion, both using RMM. The black solid line represents the true model, the blue dashed line denotes the initial model, and the red solid line indicates the inversion result.

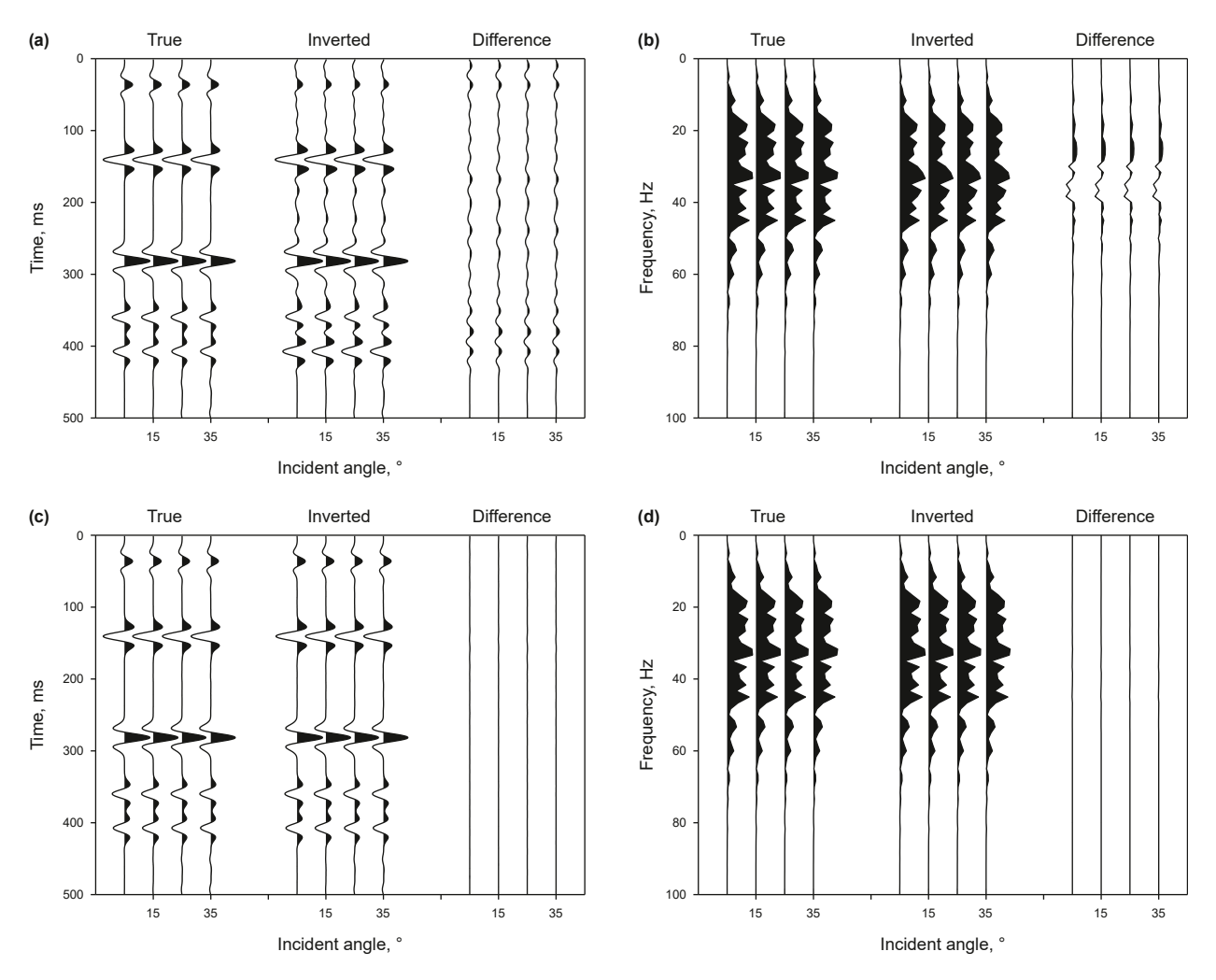


Fig. 10. Comparison of observed data and synthetic data. Time-domain waveform inversion results: (a) time-domain waveform, (b) frequency-domain amplitude spectral. Time-frequency domain joint inversion results: (c) time-domain waveform, (d) frequency-domain amplitude spectral.

results using RMM, as illustrated in Fig. 9. The black solid line denotes the true model, the blue dashed line indicates the initial model, and the red solid line represents the inversion result. Fig. 9 (a) displays the Aki approximation inversion results, where P- and S-wave velocity and density exhibit apparent jitters within the layer. Fig. 9(b) illustrates the time-domain waveform inversion results using RMM. It is evident that the inversion results exhibit minor jitters within the layer. Nonetheless, compared to the results based on the conventional Aki approximation, a significant improvement is observed. Fig. 9(c) presents the time-frequency domain joint inversion results. The inversion results exhibit excellent consistency with the true results, validating the effectiveness of the proposed method. The inversion results are substantially improved due to the constraints imposed by multidomain data, compared to single-domain inversion. To quantitatively assess the improvement, we calculated the mean squared error (MSE) between the inversion results and the true values for the three methods. As shown in Table 1, the Aki approximationbased inversion exhibits the poorest performance with the highest MSE value. In contrast, the RMM-based time-frequency joint inversion achieves the lowest MSE, confirming its superior accuracy. Moreover, the efficiency of the inversion method is also an important consideration. Compared to conventional AVO inversion, the proposed RMM-based inversion algorithm requires more computational time due to the complexity of RMM, which involves

multiple loops for frequency, angle, and layer variations. As a result, the efficiency of the inversion is closely related to these parameters. However, when compared to time-domain waveform inversion, a single iteration in the time-frequency joint inversion does not significantly increase the computational time. To address the computational cost, parallel computing could be considered to save time and make the method more accessible for large-scale applications.

Next, we analyze the discrepancies between the synthetic angle gathers generated by the RMM inversion results and the observed data, as depicted in Fig. 10. Fig. 10(a) and (b) show that the timedomain waveform traces from the true model and the inversion results exhibit a high degree of agreement. However, noticeable differences exist in their frequency-domain amplitude spectral. Therefore, relying solely on time-domain data for predicting P- and S-wave velocity and density is insufficient, and frequency domain information should also be integrated. It is crucial to ensure not only alignment in the time domain but also minimization of errors in the frequency-domain amplitude spectral. Fig. 10(c) and (d) present the comparison of the synthetic and observed data obtained from the joint inversion results in both the time and frequency domains, illustrating enhanced consistency. These results demonstrate that incorporating frequency-domain information into waveform inversion improves the accuracy of elastic parameter estimation.

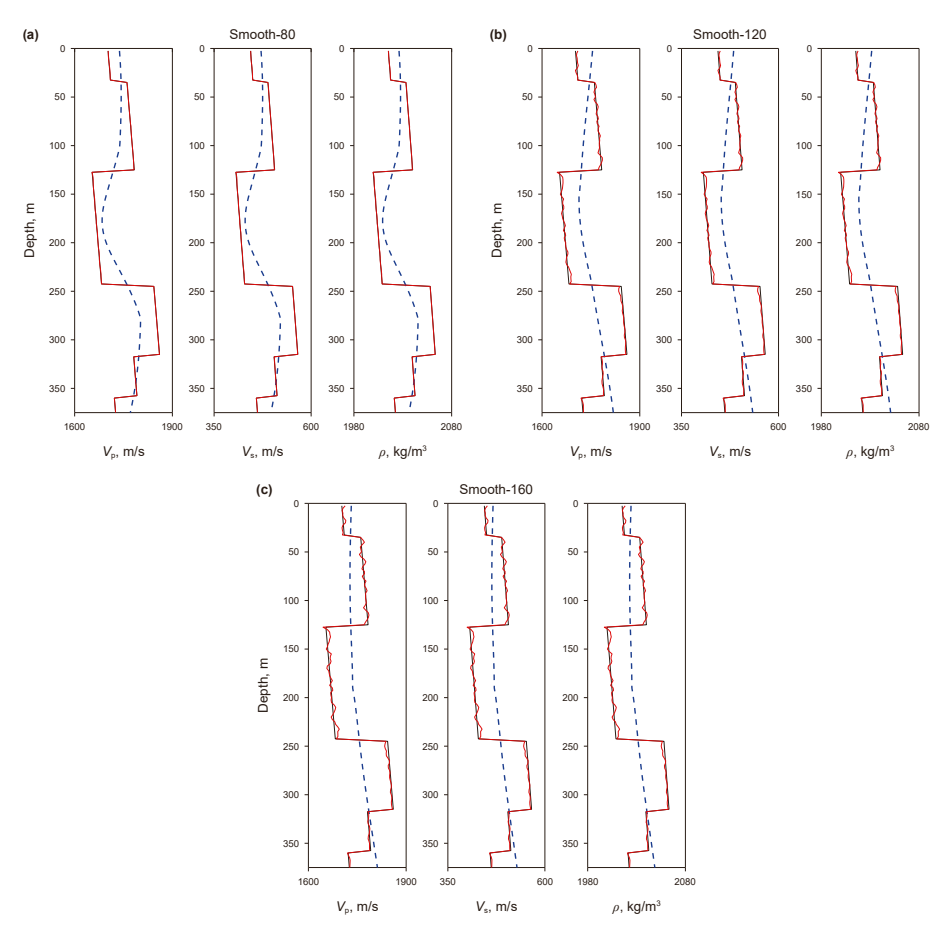


Fig. 11. Influence of initial models smoothness on inversion results: (a) 80-point smoothing (Smooth-80), (b) 120-point smoothing (Smooth-120), and (c) 160-point smoothing (Smooth-160). The black, blue, and red lines represent the true model, initial model, and inversion result, respectively.

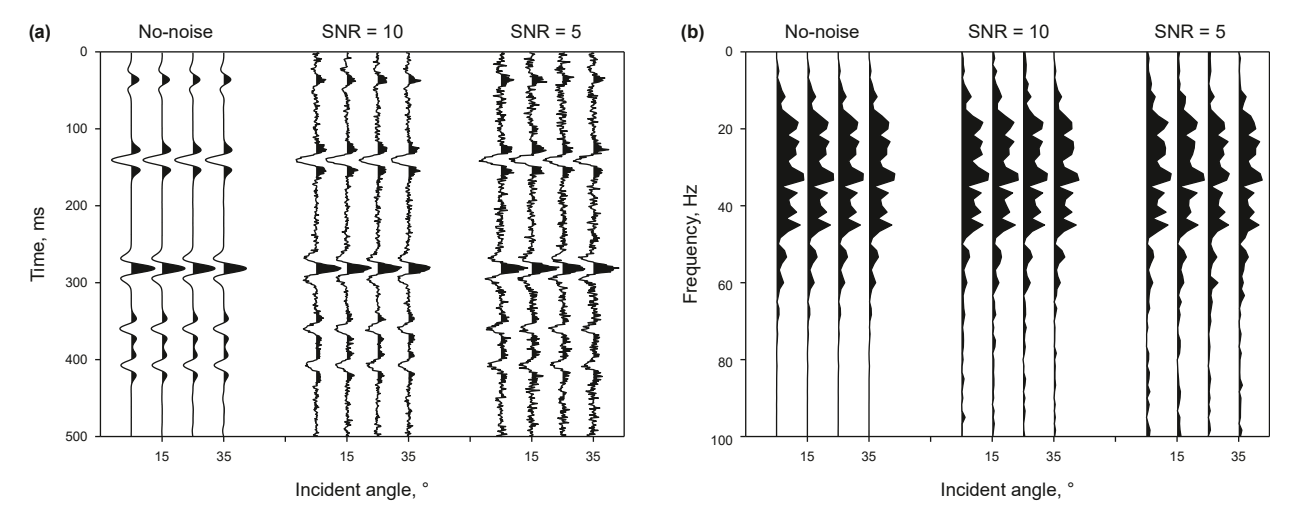


Fig. 12. Observed data under different random noise levels: (a) time-domain waveforms and (b) frequency-domain amplitude spectral.

Additionally, we explore the impact of various initial models on the time-frequency domain joint inversion results. This study utilizes a smooth function to generate the initial model with gradually increasing smoothness. Whereas the prior inversion adopted a 50-point moving average for initial model generation, the current analysis tests 80-point, 120-point and 160-point moving average. The joint inversion results are depicted in

Fig. 11. Fig. 11(a)–(c) show the inversion result based on the 80-point, 120-point and 160-point moving average, respectively. The black solid line denotes the true model, the blue dashed line indicates the initial model, and the red solid line represents the inversion results. As the smoothness of the initial model increases, the time-frequency domain joint inversion results display increasing jitter. When the initial model approximates a straight

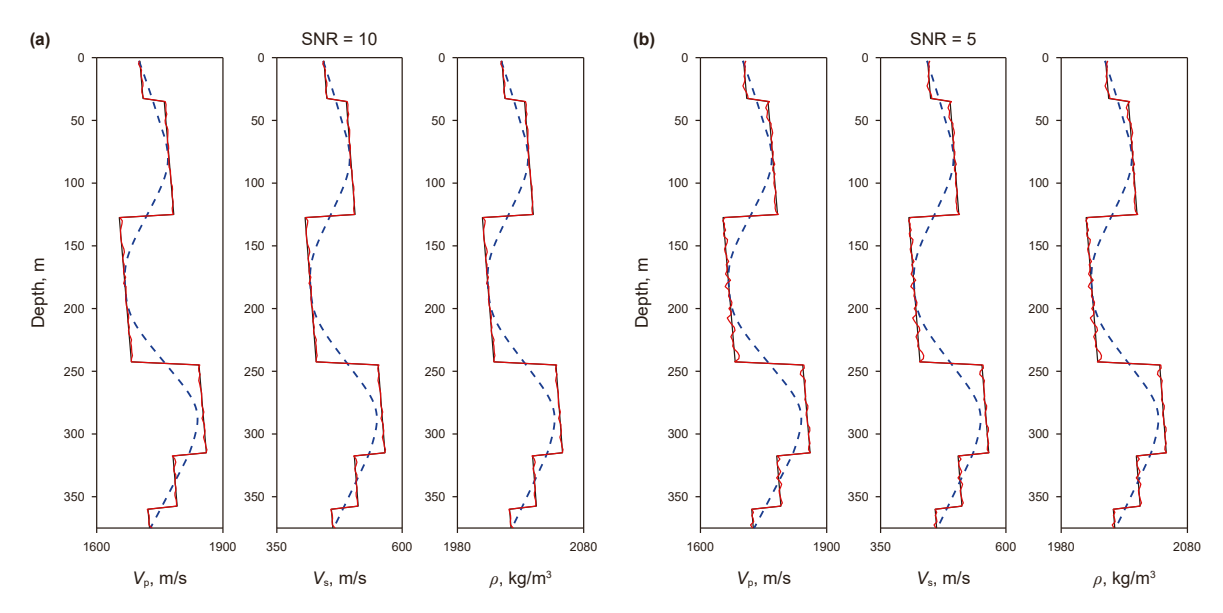


Fig. 13. Time-frequency domain joint inversion results under different random noise levels: (a) SNR = 10, (b) SNR = 5. The black, blue, and red lines represent the true model, initial model, and inversion result, respectively.

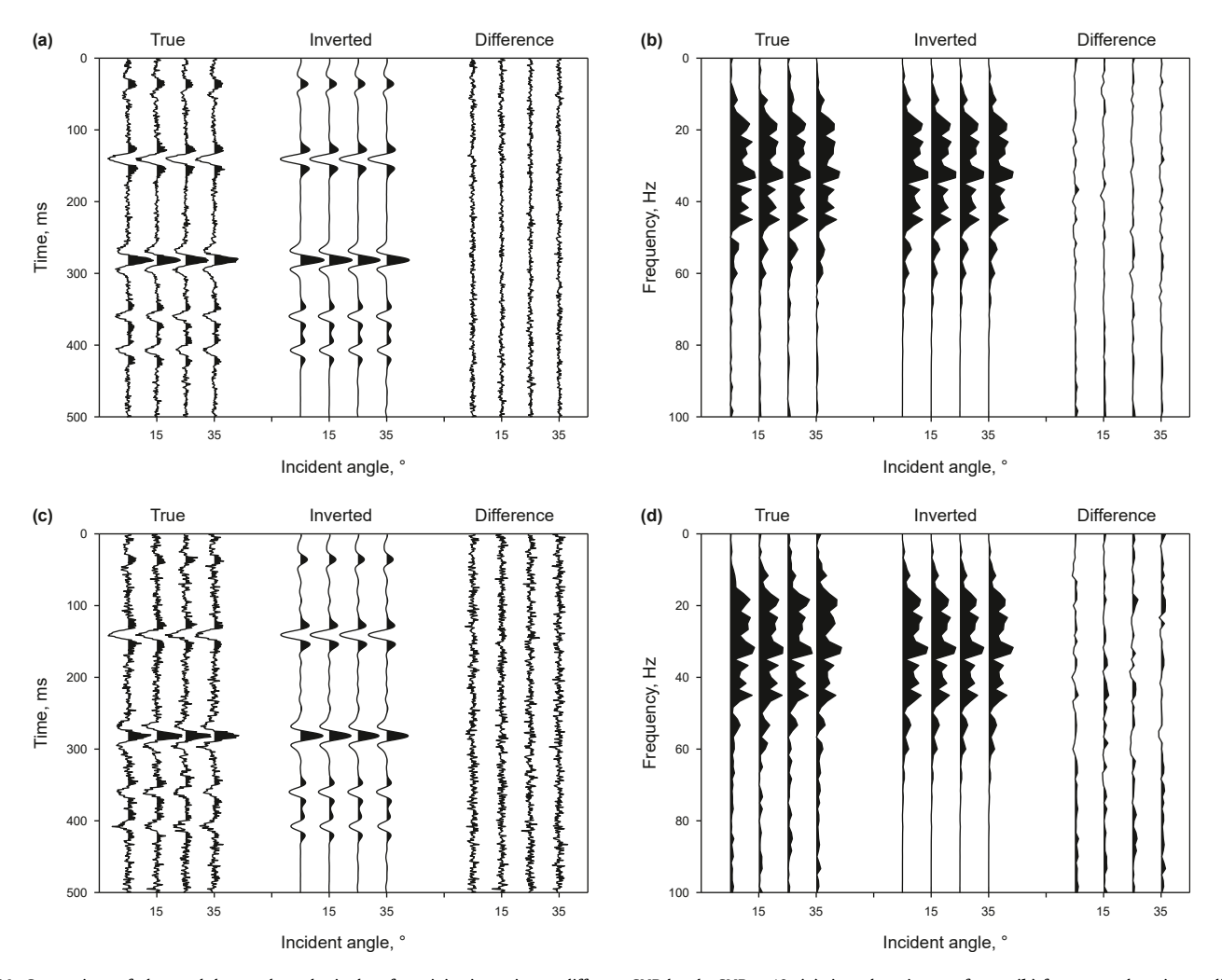


Fig. 14. Comparison of observed data and synthetic data from joint inversion at different SNR levels. SNR = 10: (a) time-domain waveforms, (b) frequency-domain amplitude spectral; SNR = 5: (c) time-domain waveforms, (d) frequency-domain amplitude spectral.

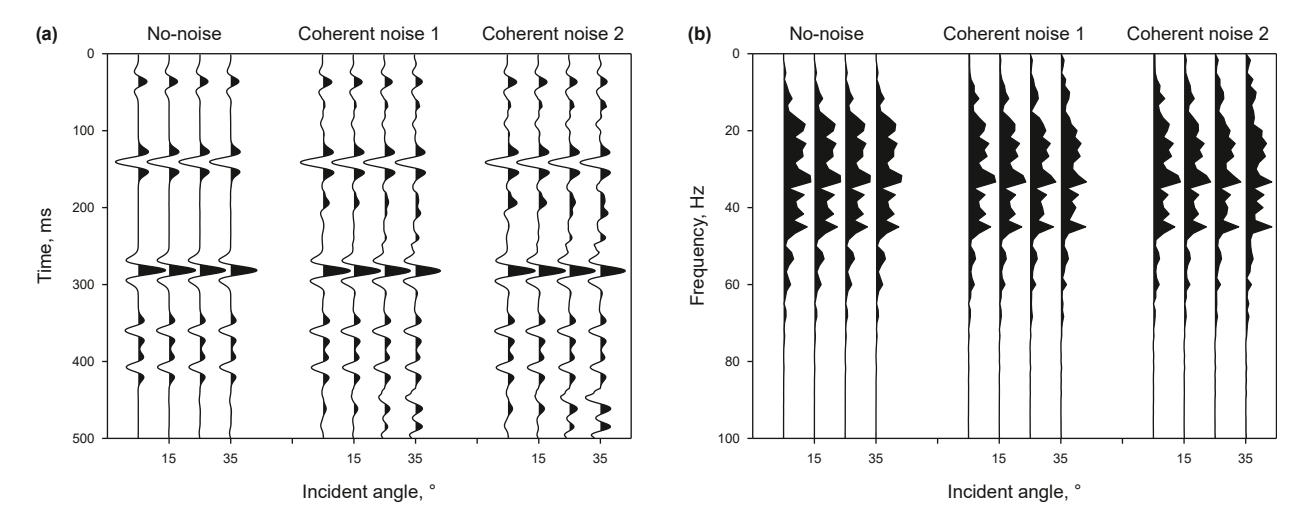


Fig. 15. Comparison of observed data with different levels of coherent noise: (a) time-domain waveform and (b) frequency-domain amplitude spectral.

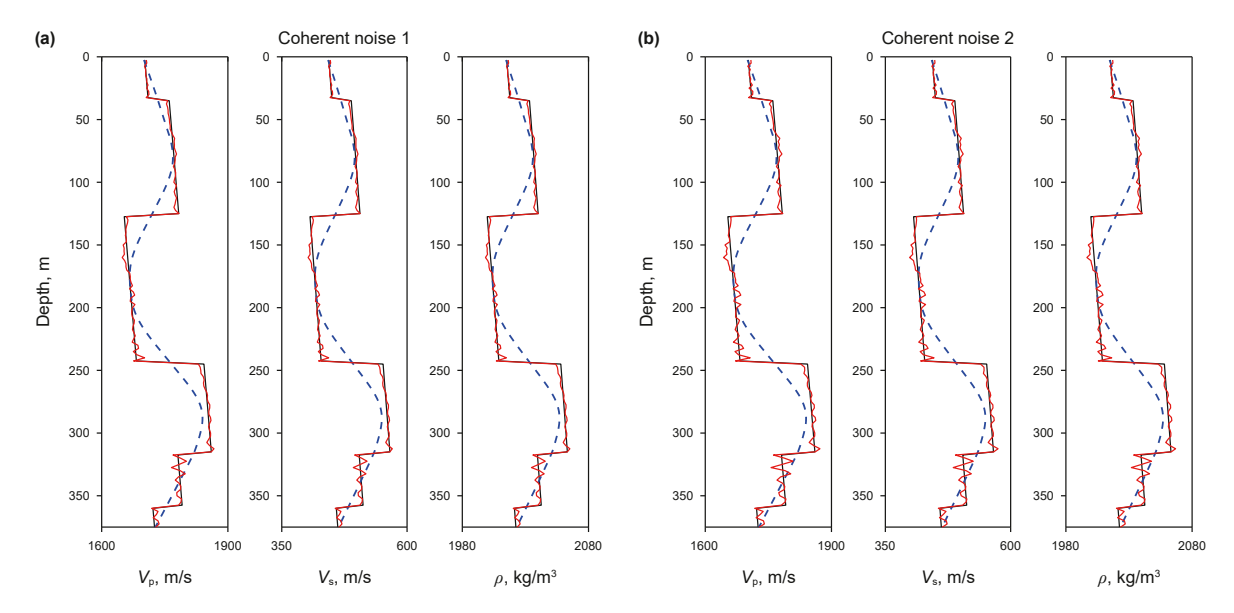


Fig. 16. Time-frequency domain joint inversion results under different levels of coherent noise (a) noise 1 and (b) noise 2. The black, blue, and red lines represent the true model, initial model, and inversion result, respectively.

line, the prediction accuracy is minimized. Nevertheless, the method remains relatively high independence from the initial model and demonstrates strong robustness.

Random noise was added to the observed data to assess the noise resistance of the proposed method, with noise intensity quantified by signal-to-noise ratio (SNR). Fig. 12 compares the observed data under three conditions: no noise, SNR = 10 and SNR = 5. Fig. 12(a) shows the time-domain waveform at different noise levels, while Fig. 12(b) presents the frequency-domain amplitude spectral under varying noise levels. Prestack timefrequency domain joint inversion was performed using observation data under various noise conditions. The results are illustrated in Fig. 13, where Fig. 13(a) and (b) present the inversion results at SNR = 10 and SNR = 5, respectively. The black solid line denotes the true model, the blue dashed line indicates the initial model, and the red solid line represents the inversion results. Despite the presence of random noise, the proposed method accurately estimates the P- and S-wave velocity and density parameters, demonstrating strong noise resistance.

Fig. 14 compares the observed data with the synthetic data derived from the joint inversion for different random noise levels. Fig. 14(a) and (b) show the comparison between the time-domain waveform data and frequency-domain amplitude spectral data at SNR = 10, respectively, while Fig. 14(c) and (d) present the results at SNR = 5. The difference represents the residual between the observed and synthetic data. Evidently, for both SNR = 10 and SNR = 5, the inversion results accurately reconstruct the waveform and amplitude spectral data. The residual between the observed and synthetic data approximates the added random noise, demonstrating the superior noise resistance of the proposed method.

Building on the random noise tests, we further explored the impact of coherent noise (primarily multiples) on inversion results. Fig. 15 compares three datasets: noise-free data, data with weak coherent noise (coherent noise 1), and data with strong coherent noise (coherent noise 2). Fig. 15(a) and (b) show the time-domain waveform and frequency-domain amplitude spectral under different noise levels, respectively. The inversion results are

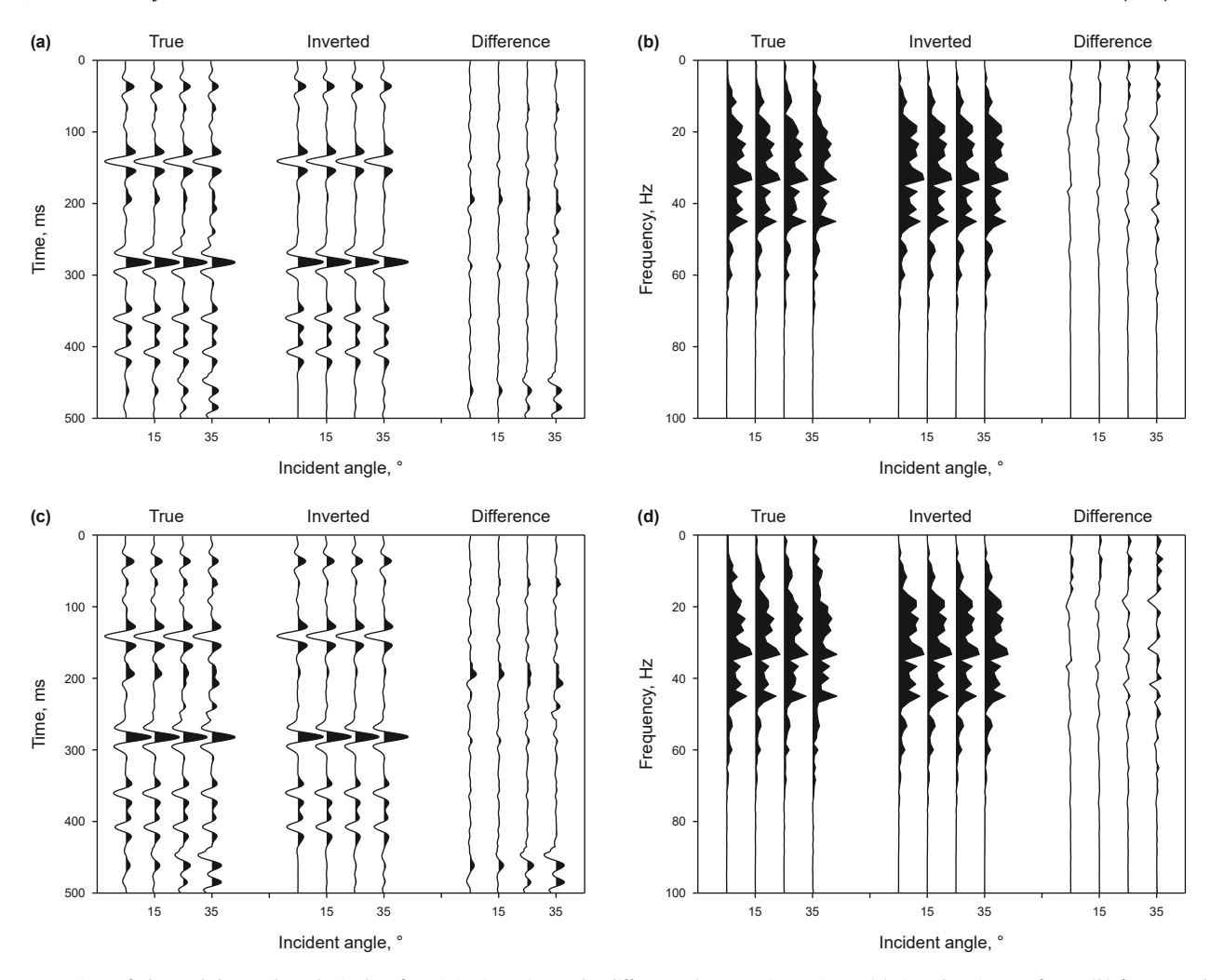


Fig. 17. Comparison of observed data and synthetic data from joint inversion under different coherent noise. Noise 1: (a) time-domain waveforms, (b) frequency-domain amplitude spectral; noise 2: (c) time-domain waveforms, (d) frequency-domain amplitude spectral.

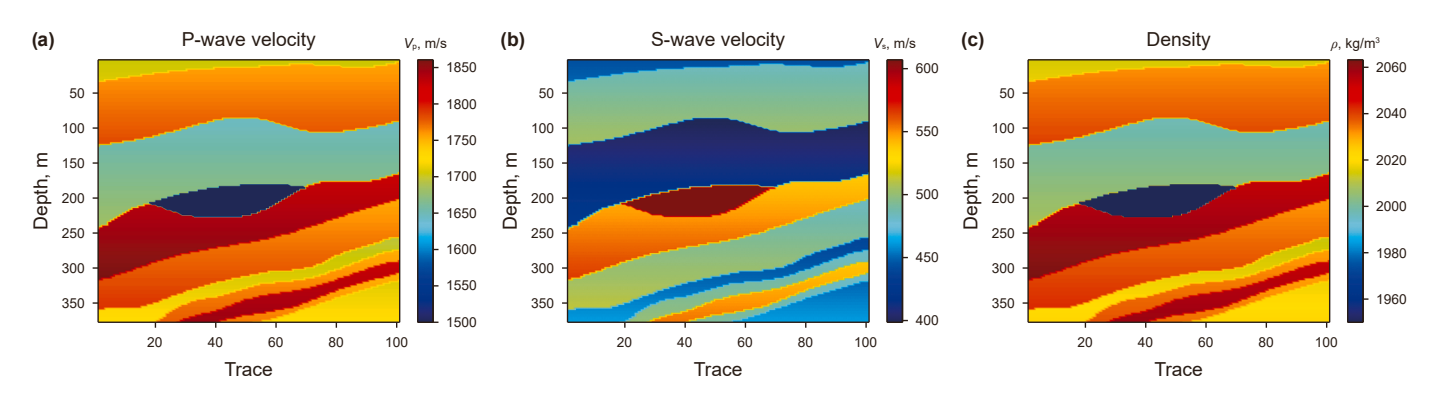


Fig. 18. Elastic parameters of a local region from the Marmousi-2 model: (a) P-wave velocity, (b) S-wave velocity, (c) density.

presented in Fig. 16, where Fig. 16(a) and (b) correspond to weak and strong coherent noise, respectively. The results indicate that as the intensity of coherent noise increases, inversion accuracy declines, with its interference effect significantly stronger than that of random noise. This is due to coherent noise exhibiting waveform characteristics rather than discrete noise points. Fig. 17 compares the observed data with synthetic data derived from joint inversion. Fig. 17(a) and (b) show the comparison between time-

domain waveform and frequency-domain amplitude spectral under weak interference, while Fig. 17(c) and (d) display the results under strong interference. These differences represent the residuals between the observed and synthetic data. Notably, the joint inversion method successfully reconstructs both waveform and spectral characteristics even in the presence of coherent noise. This robustness arises from the method's ability to accurately simulate interbed multiples, demonstrating excellent resistance to

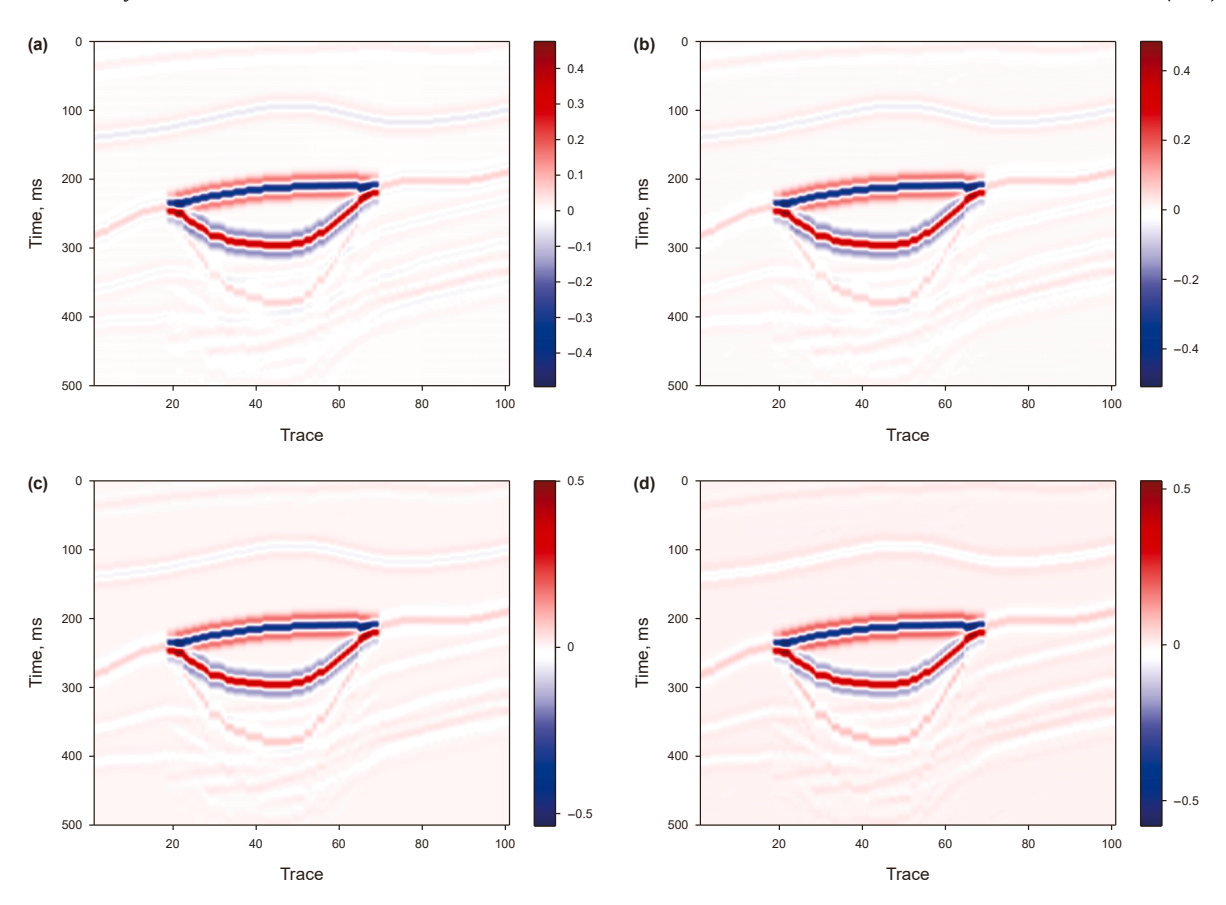


Fig. 19. Prestack angle gathers generated by forward modeling of the Marmousi-2 model at incident angles of (a) 5°, (b) 15°, (c) 25° and (d) 35°.

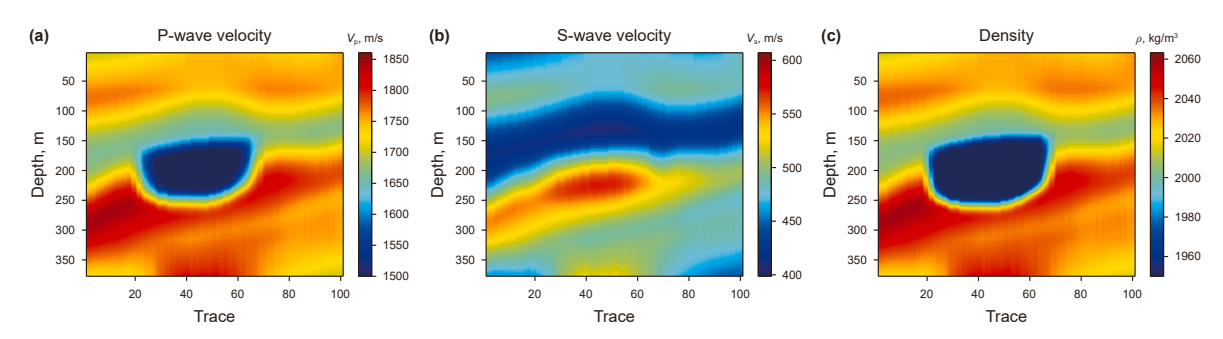


Fig. 20. Initial model of a local region from the Marmousi-2 model: (a) P-wave velocity, (b) S-wave velocity, (c) density.

coherent noise interference. It is worth emphasizing that in practical seismic data processing, coherent noise can typically be effectively suppressed through preprocessing techniques.

To further assess the efficacy of the time-frequency domain joint inversion method, we performed tests with 2D model data. The model data are extracted from a section of the Marmousi-2 model, as shown in Fig. 18. Fig. 18(a)–(c) show the P- and S-wave velocity and density, respectively. Forward modeling was performed using a 30 Hz Ricker wavelet, with the resulting prestack angle gathers for incident angles of 5°, 15°, 25°, and 35° shown in Fig. 19. Importantly, due to the significant contrast in elastic parameters between the central gas-bearing layer and the surrounding rock, distinct amplitude variations are evident in the

gathers. Fig. 20 presents the initial models for the P- and S-wave velocity, and density.

Fig. 21 shows the inversion results, with Fig. 21(a)–(c) depicting the Aki approximation-based inversion results, Fig. 21(d)–(f) presenting the time-domain waveform inversion results using RMM, and Fig. 21(g)–(i) displaying the time-frequency domain joint inversion results using RMM. It is evident that the Aki approximation-based inversion results are less effective in characterizing the gas reservoir and are significantly inferior to those from RMM, as RMM considers wave propagation effects between layers in the forward modeling. Moreover, by integrating frequency-domain information, the time-frequency domain joint inversion using RMM yields more accurate results than the time-

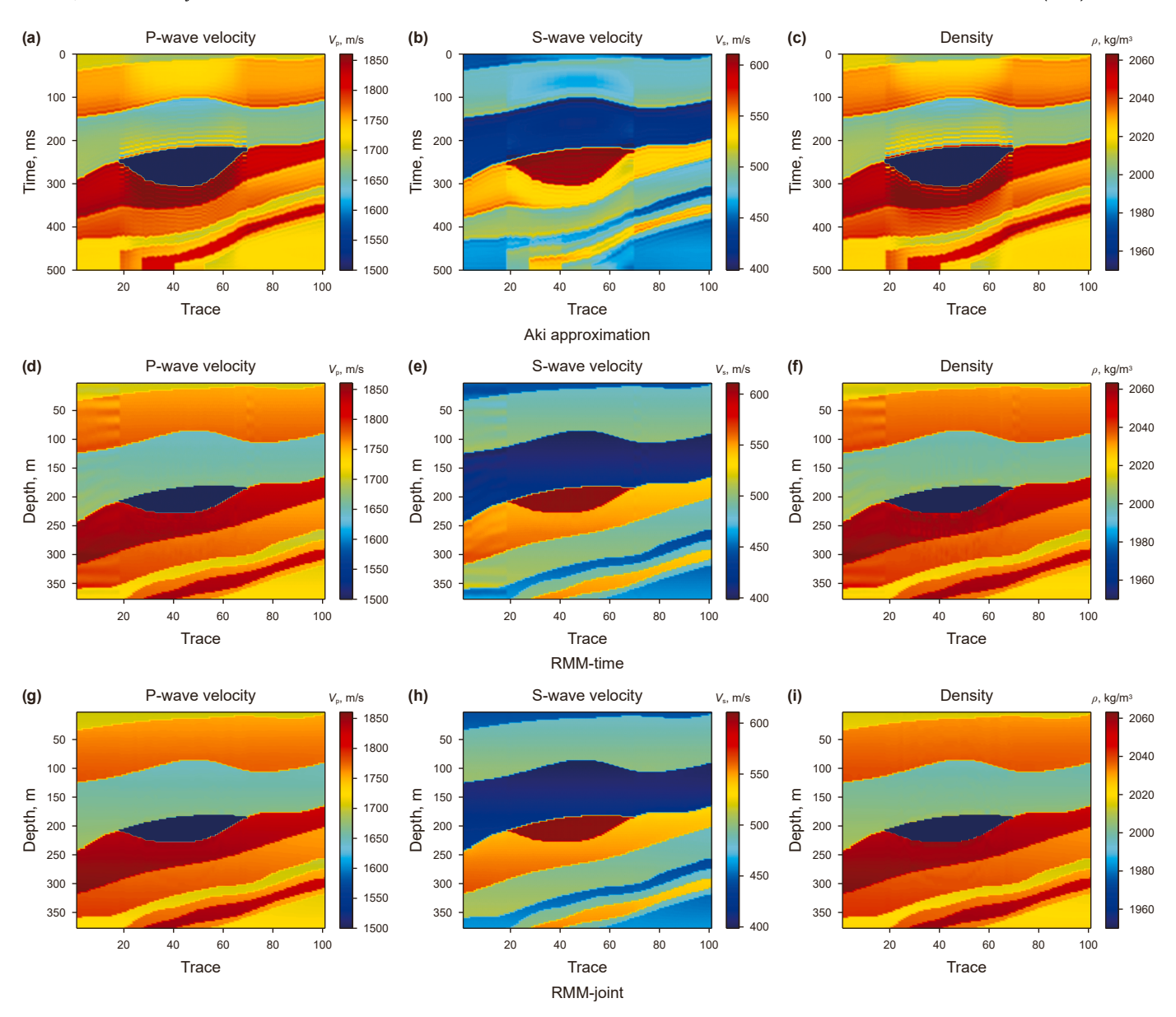


Fig. 21. Comparison of parameter prediction results for three inversion methods: prestack seismic inversion using the Aki approximation: (a) V_p , (b) V_s and (c) ρ ; prestack waveform inversion using the RMM: (d) V_p , (e) V_s and (f) ρ ; prestack time-frequency domain joint inversion using RMM: (g) V_p , (h) V_s and (i) ρ .

domain waveform inversion. Fig. 22 shows the residuals between the inversion results of different methods and the true model. Clearly, the residuals from the time-frequency domain joint inversion using RMM are the smallest, demonstrating the effectiveness of the proposed method.

4. Field data application

Finally, the prestack time-frequency domain joint inversion method was applied to field seismic data from a target area. The field seismic data are shown in Fig. 23, where the red line denotes the location of Well A. Fig. 24 shows the well-logging curve and its Backus average for Well A, with the black line representing the well-logging curve, the red line signifying the Backus-averaged result, and a sampling interval of 2 ms. The wavelet used for field data inversion is the average wavelet estimated from the

angle gathers, as shown in Fig. 25. The initial model was generated by interpolating the Backus-averaged well data along the selected horizon.

The inversion results for the profile are shown in Fig. 26, with Fig. 26(a)–(c) depicting the Aki approximation-based inversion results, Fig. 26(d)–(f) presenting the time-domain waveform inversion results using RMM, and Fig. 26(g)–(i) displaying the time-frequency domain joint inversion results using RMM. The RMM-based inversion results are more accurate in characterizing the reservoir than those from the Aki approximation. The time-frequency domain joint inversion method using RMM provides more detailed predictions than the time-domain waveform inversion method. Fig. 27 shows the inversion results at Well A, where the black line denotes the well logging curve, the green line indicates the inversion results based on the Aki approximation, the blue line represents the time-domain waveform inversion results

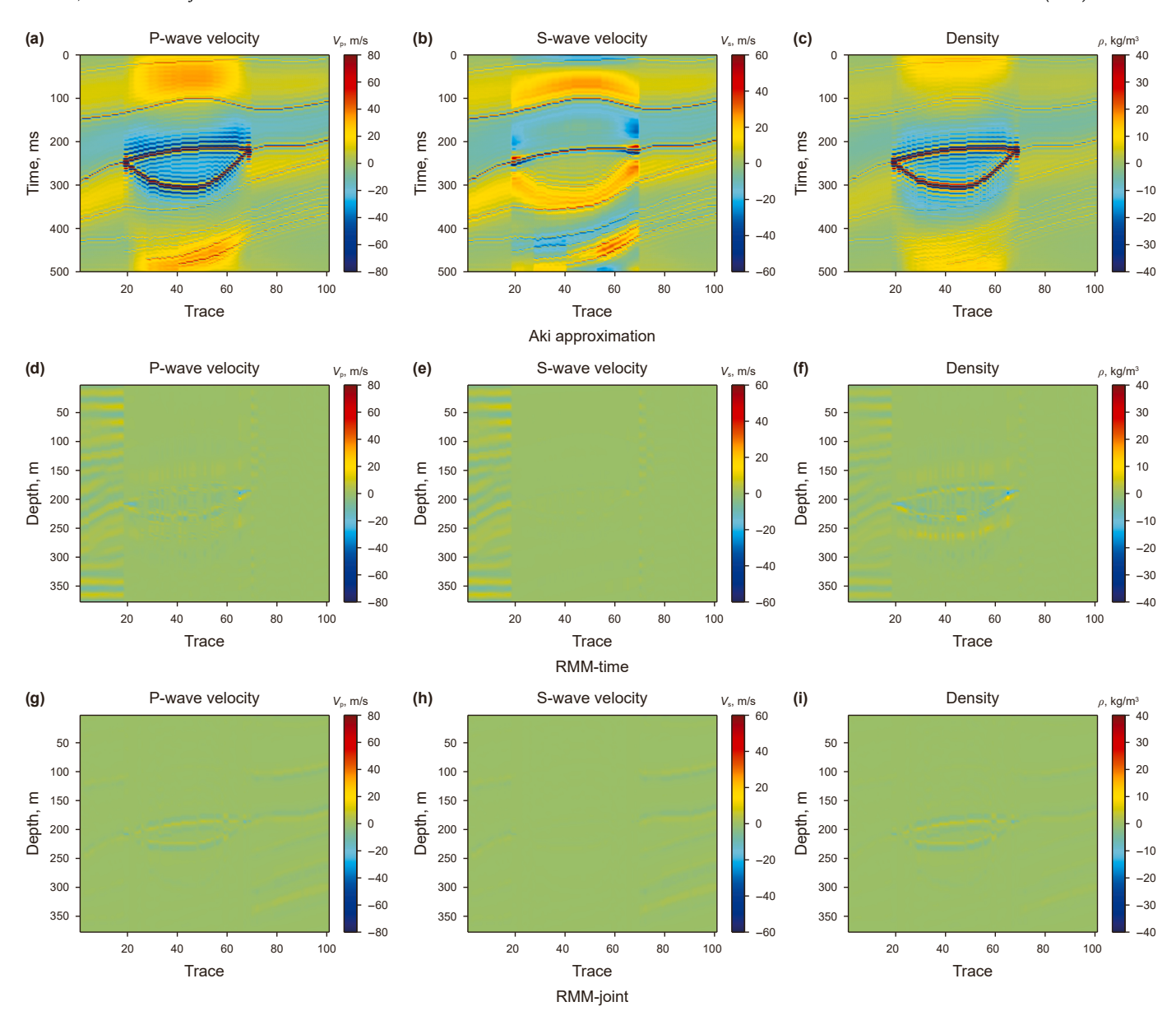


Fig. 22. Comparison of residuals between the true model and inversion results for three inversion methods: prestack seismic inversion using the Aki approximation: (a) V_p , (b) V_s and (c) ρ ; prestack waveform inversion using the RMM: (d) V_p , (e) V_s and (f) ρ ; prestack time-frequency domain joint inversion using the RMM: (g) V_p , (h) V_s and (i) ρ .

using RMM, and the red line shows the time-frequency domain joint inversion results using RMM. It is evident that the elastic parameters predicted by the proposed time-frequency domain joint inversion method are closer to the well-logging data and exhibit excellent consistency with it, demonstrating the method's effectiveness in field applications.

5. Discussion

We proposed a prestack time-frequency domain joint inversion method that demonstrates strong robustness to noise and initial model variations. However, several limitations exist due to the method relies on the layered media assumption.

First, the complexity of field data presents a significant challenge. Real logging data are inherently complex, and seismic data typically represent the superposition of waveforms from numerous thin layers, thus making it difficult to resolve blocky structures. Second, noise and uncertainties in field seismic data can obscure sharp boundaries and reduce the resolution of inversion results, as shown in Fig. 13(a) and (b). Additionally, the Gaussian prior distribution tends to yield smooth solutions, potentially weakening the ability to characterize blocky structures. Finally, while the proposed method is robust to initial model selection, an initial model closer to the true model can significantly enhance convergence speed and inversion accuracy, as shown in Fig. 11(a)–(c). Therefore, the initial model should be geologically

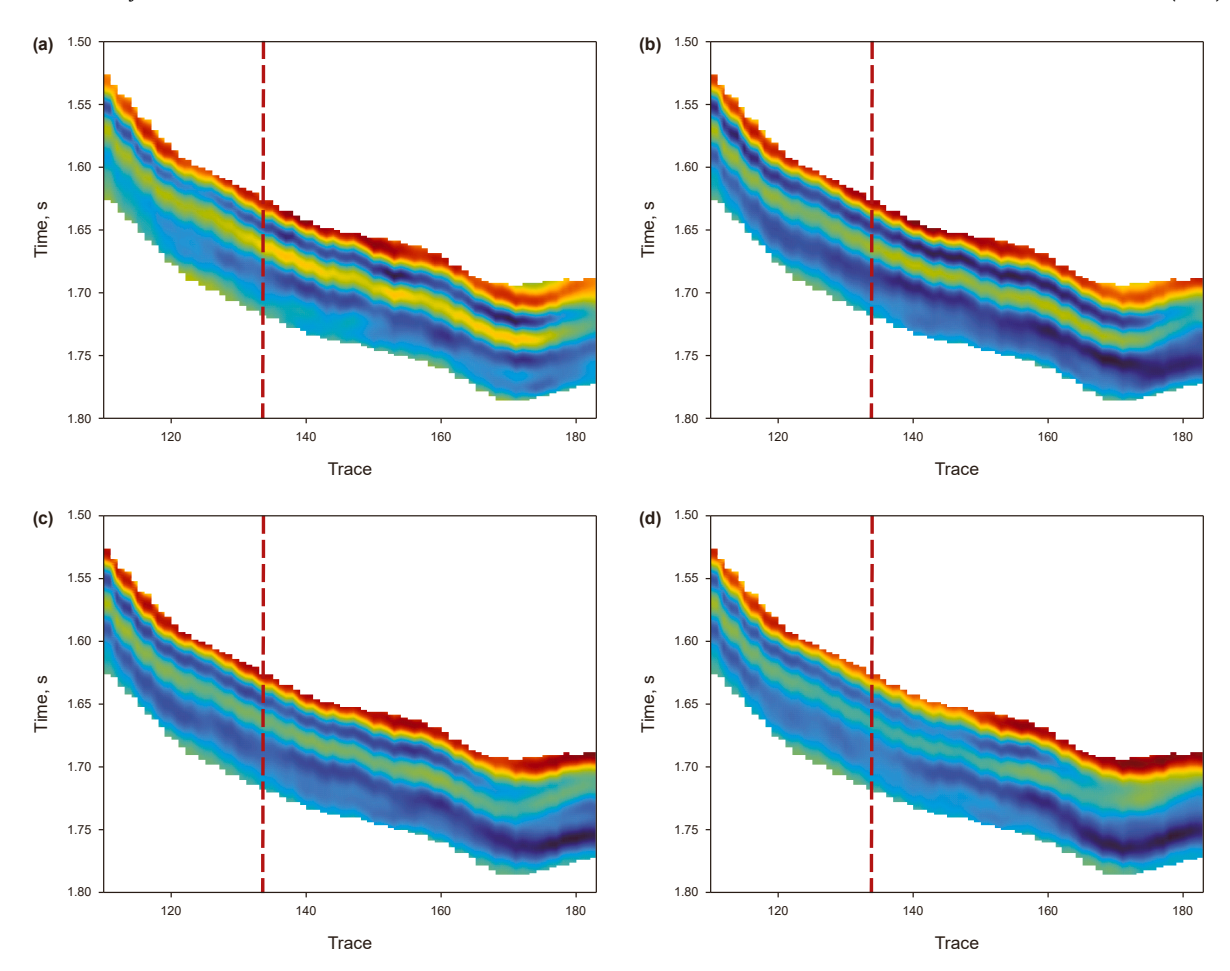


Fig. 23. Partial stacking angle gathers of the field dataset: (a) 3°–13°, (b) 11°–21°, (c) 19°–29° and (d) 27°–37°. The red dotted line indicates the position of well A.

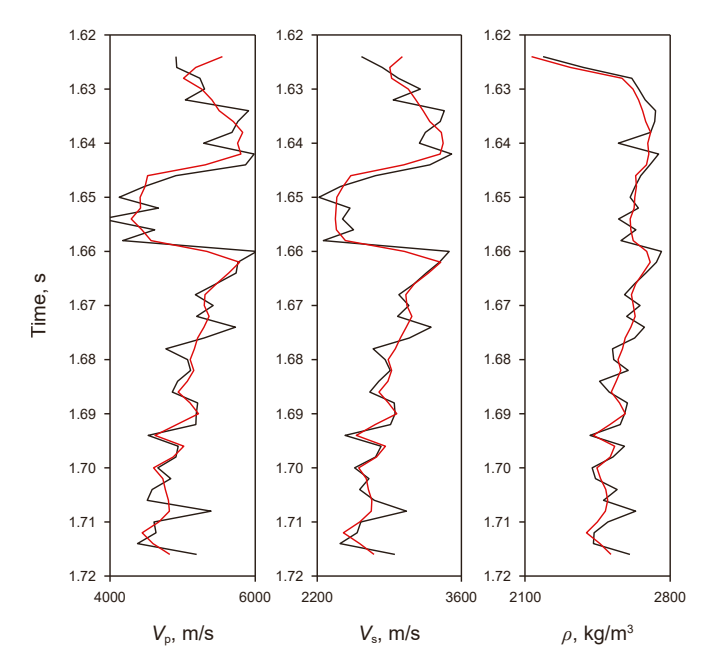


Fig. 24. Well A logging curve and Backus average results: the black solid line denotes the well curve, and the red solid line represents the Backus average.

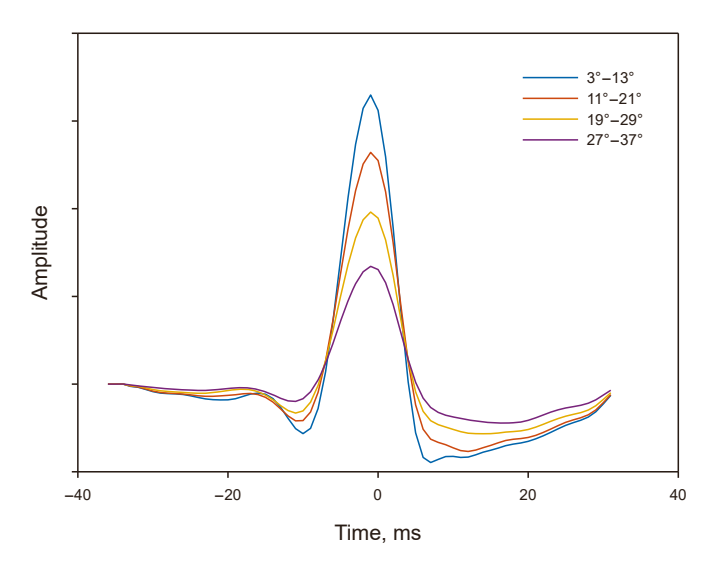


Fig. 25. Estimated wavelets from four partial stacking angle gathers.

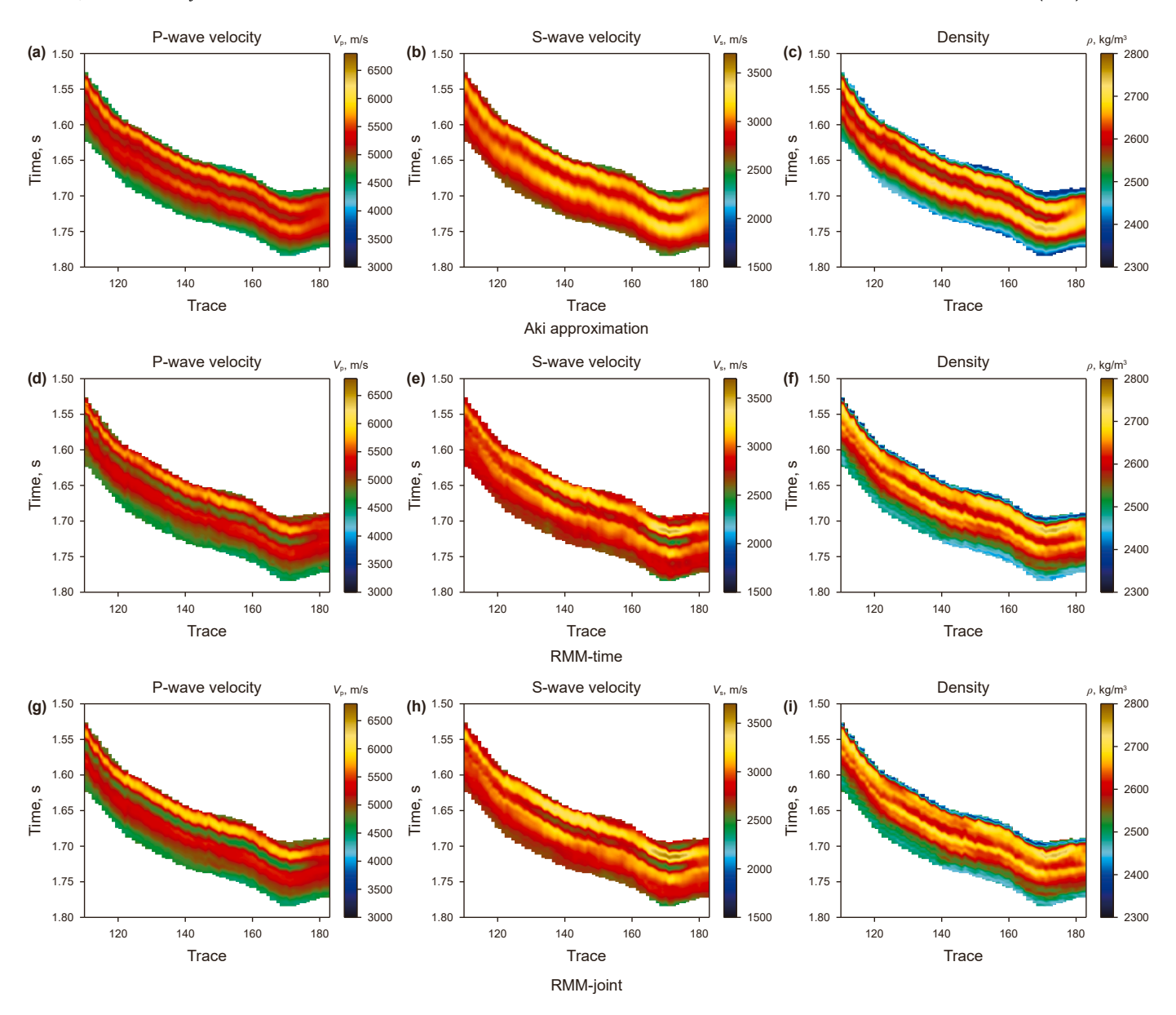


Fig. 26. Comparison of parameters prediction results for three inversion methods: prestack seismic inversion using the Aki approximation: (a) V_p , (b) V_s and (c) ρ ; prestack waveform inversion using the RMM: (d) V_p , (e) V_s and (f) ρ ; prestack time-frequency domain joint inversion using the RMM: (g) V_p , (h) V_s and (i) ρ .

plausible and consistent with prior subsurface structure knowledge to ensure a reasonable inversion starting point.

Despite these limitations, the results from our method remain reasonable and reliable. Future work could focus on addressing these challenges through advanced noise suppression techniques, more sophisticated prior distributions, and initial model selection optimization strategies.

6. Conclusion

This paper presents a prestack time-frequency domain joint inversion method for layered media within a Bayesian framework. The method uses Gauss-Newton iteration to estimate key parameters, including P- and S-wave velocity, and density. In the forward modeling stage, RMM is used to capture wave propagation characteristics in layered media, such as multiple reflections and

transmission losses. By integrating both time-domain waveform and frequency-domain data in the inversion, the method provides significant advantages in noise resistance and resolution.

Experimental results from synthetic and field data show that the proposed method significantly outperforms conventional AVA inversion and time-domain waveform inversion in terms of accuracy, resolution, and noise resistance. The method shows strong stability under varying initial models and can provide reliable predictions even under low SNR and strong coherent noise interference. Furthermore, comparisons with well-logging data validate the practical applicability of our method for high-precision reservoir characterization.

Future research could focus on extending the method to more complex media, such as anisotropic or viscoelastic media, where frequency-domain information may offer unique insights.

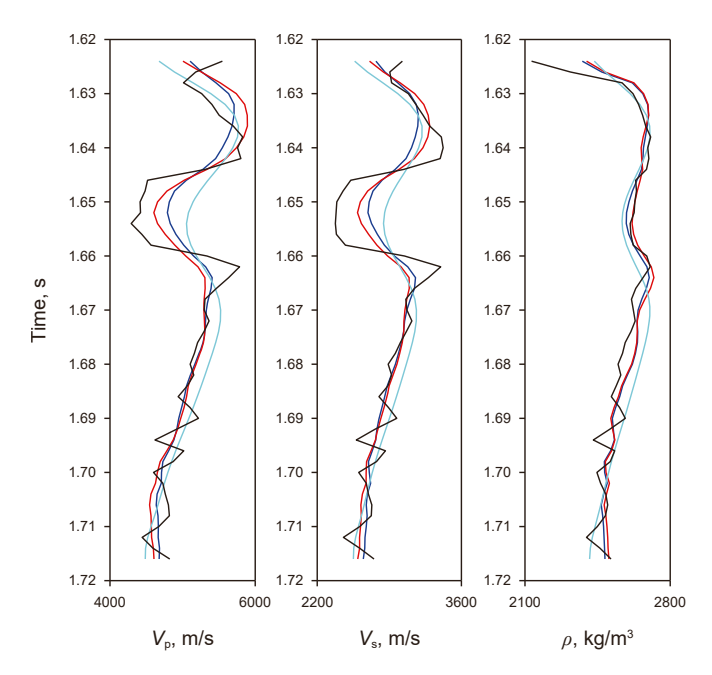


Fig. 27. Comparison of inversion results for three methods at Well A: the black line denotes the logging curve, the green line represents the inversion results using the Aki approximation, the blue line indicates the time-domain waveform inversion results using the RMM, and the red line shows the time-frequency domain joint inversion results using the RMM.

CRediT authorship contribution statement

Zheng-Yang Kuai: Writing – review & editing, Writing – original draft, Methodology, Investigation. **Dan-Ping Cao:** Writing – review & editing, Supervision, Conceptualization. **Chao Jin:** Writing – review & editing, Supervision, Conceptualization.

Declaration of competing interest

The authors declare that they have no known competing financial interests or personal relationships that could have appeared to influence the work reported in this paper. The authors acknowledge there are no conflicts of interest recorded.

Acknowledgments

We would like to acknowledge the sponsorship of National Natural Science Foundation of China (42325403) and DeepEarth Probe and Mineral Resources Exploration - National Science and Technology Major Project of China (2024ZD1004201).

References

Aki, K., Richards, P.G., 2002. Quantitative Seismology. University Science Books, California, USA.

Alemie, W., Sacchi, M.D., 2011. High-resolution three-term AVO inversion by means of a Trivariate Cauchy probability distribution. Geophysics 76 (3), R43–R55. https://doi.org/10.1190/1.3554627.

Amundsen, L., Ursin, B., 1991. Frequency-wavenumber inversion of acoustic data. Geophysics 56 (7), 1027–1039. https://doi.org/10.1190/1.1443111.

Buland, A., More, H., 2003. Bayesian linearized AVO inversion. Geophysics 68 (1), 185–198. https://doi.org/10.1190/1.1543206.

Carcione, J.M., 1990. Wave propagation in anisotropic linear viscoelastic media: theory and simulated wavefields. Geophys. J. Int. 101 (3), 739–750. https://doi.org/10.1111/j.1365-246X.1990.tb05580.x.

Fryer, G.J., Frazer, L.N., 1987. Seismic waves in stratified anisotropic media—II. Elastodynamic eigensolutions for some anisotropic systems. Geophys. J. Int. 91 (1), 73–101. https://doi.org/10.1111/j.1365-246X.1987.tb05214.x. Fuchs, K., 1968. The reflection of spherical waves from transition zones with arbitrary depth-dependent elastic moduli and density. J. Phys. Earth 16, 27–41. https://doi.org/10.4294/JPE1952.16.SPECIAL_27.

Fuchs, K., Müller, G., 1971. Computation of synthetic seismograms with the reflectivity method and comparison with observations. Geophys. J. Int. 23 (4), 417–433. https://doi.org/10.1111/j.1365-246X.1971.tb01834.x.

Gilbert, F., Backus, G.E., 1966. Propagator matrices in elastic wave and vibration problems. Geophysics 31 (2), 326–332. https://doi.org/10.1190/1.1439771.

Haskell, N.A., 1953. The dispersion of surface waves on multilayered media. Bull. Seismol. Soc. Am. 43 (1), 17–34. https://doi.org/10.1785/BSSA0430010017.

Kennett, B.L.N., 2009. Seismic Wave Propagation in Stratified Media, second ed. ANU Press, Canberra, Australia.

Kennett, B.L.N., Kerry, N.J., 1979. Seismic waves in a stratified half space. Geophys. J. Int. 57 (3), 557–583. https://doi.org/10.1111/j.1365-246X.1979.tb06779.x.

Kennett, B.L.N., 1974. Reflections, rays, and reverberations. Bull. Seismol. Soc. Am. 64 (6), 1685–1696. https://doi.org/10.1785/BSSA0640061685.

Li, T., Mallick, S., 2015. Multicomponent, multi-azimuth pre-stack seismic waveform inversion for azimuthally anisotropic media using a parallel and computationally efficient non-dominated sorting genetic algorithm. Geophys. J. Int. 200 (2), 1136–1154. https://doi.org/10.1093/gji/ggu445.

Lin, K., Zhao, L., Wen, X.T., et al., 2023. Time-frequency mixed domain multi-trace simultaneous inversion method. Geoenergy Sci. Eng. 230, 212164. https://doi. org/10.1016/j.geoen.2023.212164.

Liu, H.X., Li, J.Y., Chen, X.H., et al., 2016. Amplitude variation with offset inversion using the reflectivity method. Geophysics 81 (4), R185–R195. https://doi.org/ 10.1190/geo2015-0332.1.

Lu, J., Yang, Z., Wang, Y., et al., 2015. Joint PP and PS AVA seismic inversion using exact Zoeppritz equations. Geophysics 80 (5), R239–R250. https://doi.org/ 10.1190/geo2014-0490.1.

Lu, Y.X., Peng, S.P., Cui, X.Q., et al., 2019. Thin-bed inversion using pre-stack seismic data. SEG Tech. Progr. Expand. Abstr. https://doi.org/10.1190/segam2019-3214870 1

Luo, C., Ba, J., Carcione, J.M., et al., 2020. Joint PP and PS pre-stack seismic inversion for stratified models based on the propagator matrix forward engine. Surv. Geophys. 41, 987–1028. https://doi.org/10.1007/s10712-020-09605-5.

Mallick, S., 1999. Some practical aspects of prestack waveform inversion using a genetic algorithm: an example from the east Texas Woodbine gas sand. Geophysics 64 (2), 326–336. https://doi.org/10.1190/1.1444538.

Mallick, S., 2007. Amplitude-variation-with-offset, elastic-impedence, and wave-equation synthetics—a modeling study. Geophysics 72 (1), C1–C7. https://doi.org/10.1190/1.2387108.

Mallick, S., Adhikari, S., 2015. Amplitude-variation-with-offset and prestack-waveform inversion: a direct comparison using a real data example from the Rock Springs Uplift, Wyoming, USA. Geophysics 80 (2), B45–B59. https://doi.org/10.1190/geo2014-0233.1

Marfurt, K.J., Kirlin, R.L., 2001. Narrow-band spectral analysis and thin-bed tuning. Geophysics 66 (4), 1274–1283. https://doi.org/10.1190/1.1487075.

Padhi, A., Mallick, S., 2014. Multicomponent pre-stack seismic waveform inversion in transversely isotropic media using a non-dominated sorting genetic algorithm. Geophys. J. Int. 196 (3), 1600–1618. https://doi.org/10.1093/gji/ggt460.

Partyka, G., Gridley, J., Lopez, J., 1999. Interpretational applications of spectral decomposition in reservoir characterization. Lead. Edge 18 (3), 353–360. https://doi.org/10.1190/1.1438295.

Puryear, C.I., Castagna, J.P., 2008. Layer-thickness determination and stratigraphic interpretation using spectral inversion: theory and application. Geophysics 73 (2), R37–R48. https://doi.org/10.1190/1.2838274.

Rubino, J.G., Velis, D., 2009. Thin-bed prestack spectral inversion. Geophysics 74 (4), R49–R57. https://doi.org/10.1190/1.3148002.

Sen, M.K., Stoffa, P.L., 1991. Nonlinear one-dimensional seismic waveform inversion using simulated annealing. Geophysics 56 (10), 1624–1638. https://doi.org/ 10.1190/1.1442973.

Sen, M.K., Roy, I.G., 2003. Computation of differential seismograms and iteration adaptive regularization in prestack waveform inversion. Geophysics 68 (6), 2026–2039. https://doi.org/10.1190/1.1635056.

Shuey, R.T., 1985. A simplification of the Zoeppritz equations. Geophysics 50 (4), 609–614. https://doi.org/10.1190/1.1441936.

Thomson, W.T., 1950. Transmission of elastic waves through a stratified solid medium. J. Appl. Phys. 21 (2), 89–93. https://doi.org/10.1063/1.1699629.

Yang, C., Wang, Y., 2022. Joint PP-PS seismic prestack inversion of thin-bed reservoirs. J. Geophys. Eng. 19 (4), 897–913. https://doi.org/10.1093/jge/gxac060.

Yang, Z., Lu, J., 2020. Thin interbed AVA inversion based on a fast algorithm for reflectivity. Acta Geophys. 68 (4), 1007–1020. https://doi.org/10.1007/s11600-020-00448-7.

Yin, X.Y., Li, K., Zong, Z.Y., et al., 2017. Seismic inversion in joint time-frequency domain based on Bayesian scheme. Geophys. Prospect. Pet. 56 (2), 250–260. https://doi.org/10.3969/j.issn.1000-1441.2017.02.012 (in Chinese).

Zhao, H.S., Ursin, B., Amundsen, L., 1994. Frequency-wavenumber elastic inversion of marine seismic data. Geophysics 59 (12), 1868–1881. https://doi.org/10.1190/11443574

Zhao, L., Lin, K., Wen, X.T., et al., 2023. The 3-D global prestack seismic inversion in the time–frequency mixed domain. IEEE Trans. Geosci. Rem. Sens. 61, 1–15. https://doi.org/10.1109/TGRS.2023.3282250.

Zoeppritz, K., 1919. On reflection and propagation of seismic waves. Gottinger Nachrichten 1, 66–84.